UCLA
UCLA Electronic Theses and Dissertations

Title
Investigating Controlled Delivery of Biomolecules for Therapeutic and Diagnostic Applications

Permalink
https://escholarship.org/uc/item/0pn9n0wd

Author
Pan, April Annyee

Publication Date
2017

Peer reviewed|Thesis/dissertation

UNIVERSITY OF CALIFORNIA

Los Angeles

Investigating Controlled Delivery of Biomolecules for Therapeutic and Diagnostic Applications

A thesis submitted in partial satisfaction

of the requirements for the degree Master of Science

in Bioengineering

by

April Pan

2017

ABSTRACT OF THE THESIS

Investigating Controlled Delivery of Biomolecules for Therapeutic and Diagnostic Applications

by

April Pan

Master of Science in Bioengineering

University of California, Los Angeles, 2017

Professor Daniel T. Kamei, Chair

This thesis focused on developing controlled delivery technologies to address *both* therapeutic and diagnostic applications. In the area of therapeutics, controlled delivery of anti-cancer agents to tumor sites have the potential to increase efficacy and decrease toxic side effects. With regard to diagnostics, controlled delivery of the target molecule, as well as signal enhancement reagents, to a detection zone can improve detection limits and further distinguish the difference between the signal and the background.

Cancer is the second leading cause of death in the United States. Though conventional treatments such as chemotherapy are effective, they frequently result in off-target cytotoxic effects.

There is thus a significant need to develop methodologies to achieve controlled delivery of therapeutic agents to tumor sites. To address this need, our research group has previously studied the transferrin (Tf) trafficking pathway, which is a promising mechanism for use in targeted cancer therapy due to the overexpression of transferrin receptors (TfRs) on cancerous cells. Our research group has developed a mathematical model of the Tf/TfR trafficking pathway to improve the efficiency of Tf as a drug carrier. By using diphtheria toxin (DT) as a model toxin, our laboratory discovered that mutating the Tf protein to change its iron release rate improves cellular association and efficacy of the drug. Though this was an improvement upon using wild-type Tf as the targeting ligand, conjugated toxins like DT are unfortunately still highly cytotoxic at off-target sites.

In this work, we address this hurdle in cancer research by developing a mathematical model to predict the efficacy and selectivity of Tf conjugates that use an alternative toxin. For this purpose, we have chosen to study a mutant of DT, cross-reacting material 107 (CRM107). First, we developed a mathematical model of the Tf-DT trafficking pathway by extending our Tf/TfR model to include intracellular trafficking via DT and DT receptors. Using this mathematical model, we subsequently investigated the efficacy of several conjugates in cancer cells: DT and CRM107 conjugated to wild-type Tf, as well as to our engineered mutant Tf proteins (K206E/R632A Tf and K206E/R534A Tf). We also investigated the selectivity of mutant Tf-CRM107 against non-neoplastic cells. Through the use of our mathematical model, we predicted that (i) mutant Tf-CRM107 exhibits a greater cytotoxicity than wild-type Tf-CRM107 against cancerous cells, (ii) this improvement was more drastic with CRM107 conjugates than with DT conjugates, and (iii) mutant Tf-CRM107 conjugates were selective against non-neoplastic cells. These predictions were validated with *in vitro* cytotoxicity experiments, demonstrating that the mutant Tf-CRM107

conjugate is indeed a more suitable therapeutic agent. Validation from *in vitro* experiments also confirmed that such whole-cell kinetic models can be useful in cancer therapeutic design.

This thesis also presents the investigation of controlled biomolecule delivery for diagnostic applications. Specifically, this thesis investigates the diagnosis of chlamydia, the most common bacterial sexually transmitted infection worldwide. Because it is typically asymptomatic and frequently progresses to serious complications, there is a significant need to develop a rapid diagnostic test for improved screening. The lateral-flow immunoassay (LFA) is an inexpensive paper-based immunoassay that has such potential, but it is limited in sensitivity. Methodologies such as enzymatic signal enhancement can therefore improve the sensitivity of the LFA. However, these enhancement techniques require multiple user steps, and previous attempts to integrate these processes into the LFA in a simple format have been largely unsuccessful. There is thus a need to achieve precise fluidic manipulations and controlled delivery of biomolecules and reagents to condense multistep assays into an automated, user-friendly format. Our group has previously investigated aqueous two-phase systems (ATPSs) for the controlled delivery of biomolecules in LFAs. Specifically, our laboratory has demonstrated the novel application of ATPSs to improve LFAs by pre-concentrating target biomarkers and automatically delivering only the concentrated portion to the detection zone. Macroscopic phase separation behavior was also shown to be tunable by changing the 3D architectural design of the paper and subsequently the size of the leading phase.

In this thesis, more advanced control of biomolecule delivery in paper-based immunoassays and subsequent improvement of LFA sensitivity are presented. We demonstrate (i) the investigation of ATPS to mediate automated, sequential delivery signal enhancement reagents, and (ii) the development of a housing to achieve fine tuning of conjugate release and fluid flow of the ATPS through the paper matrix. Specifically, the partitioning of a model enzyme, alkaline

phosphatase (ALP), and its substrates, nitroblue tetrazolium 5-bromo-4-chloro-3-idolyphosphate (NBT/BCIP), into opposite phases prevented premature enzymatic signal enhancement, and the phase separation behavior of ATPS on a paper matrix drove automated sequential delivery. Furthermore, the design of an acrylic housing prevented flow inconsistencies from evaporation and provided sufficient pressure contact to improve fluid flow for the paper-based test. An automated, single-step test was thus successfully developed. In the future, this biomolecule delivery technology can be extended to other diagnostic platforms and multistep assay systems.

The thesis of April Pan is approved.

Wentai Liu

Benjamin M. Wu

Daniel T. Kamei, Committee Chair

University of California, Los Angeles

2017

Dedicated to my family.

Table of Contents

Acknowledgments

This thesis would not be possible without the support of many individuals. First and foremost, I would like to thank my advisor and greatest teacher, Dr. Daniel T. Kamei. Your love and passion for teaching and mentorship is absolutely unparalleled, and I truly would not be the researcher I am today without you. I have grown so much under your guidance – not only in science, but also in character. Thank you for constantly challenging me and inspiring me to become a better individual.

I would also like to thank my graduate student colleagues. Daniel "Brad" Bradbury, thank you for being a wonderful mentor. I have learned so much from you, and it was truly a pleasure to work with you. David Pereira, thank you for supporting me and having a great sense of humor. Sherine Cheung, thank you for being such a caring individual and for always giving me amazing advice.

A huge thank you also goes out to the rest of the Kamei Lab family, all of whom I could not imagine these last two years without – Garrett, for mentoring me and for your jokes; Phuong, for being the first to welcome me when I first joined and for training me; Sam Cheng and Alison, for supporting me through difficult times; Allison, for being like a big sister to me; Chloe, for always challenging me; Justin and Eumene, for being the dynamic duo that always puts a smile on my face – the list goes on. Thank you all. I feel very lucky to have been able to meet and be a part of such an incredible group of people.

Chapter 2 is a version of D.J. Yoon, K.Y. Chen, A.M. Lopes, A.A. Pan, J. Shiloach, A.B. Mason, and D.T. Kamei, "Mathematical Modeling of Mutant Tf-CRM107 Molecular Conjugates for Cancer Therapy." *J. Theor. Biol.* 2017, **416**: 88-98. Copyright © 2017 Elsevier B.V. D.T. Kamei was the director of research for this article. Experiments and modeling were conducted by

1. Motivation and Background

1.1. Targeted Cancer Therapy

1.1.1. Introduction: Cancer

Cancer is the second leading cause of death in the United States, with an estimation of over 1.6 million new cases and over 600,000 deaths in 2017 alone [1]. The leading type of cancer in men is prostate cancer, with over 161,000 expected diagnoses in 2017, and the leading type of cancer in women is breast cancer, with over 252,000 expected diagnoses [1]. Although traditional cancer therapies such as chemotherapy have been effective in treating cancer, the cytotoxicity of chemotherapeutic agents results in many off-target side effects [2]. In addition, the resulting systemic toxicity to host cells limits the dose that can be used, which narrows the therapeutic window of these anticancer drugs. There is thus a significant need to develop targeted cancer therapies for specific treatment of cancer cells while limiting off-target side effects.

1.1.2. Current Methods of Controlled Biomolecule Delivery for Therapeutic Applications

One method of controlled delivery for targeted tumor therapy involves the use of monoclonal antibodies. In this approach, monoclonal antibodies that are specific to markers on cancer cell surfaces but not to critical normal host cell surfaces are used [3]–[5]. The specificity that is conferred can ideally allow the use of more potent drugs that would otherwise be too toxic [3]. Since monoclonal antibodies by themselves typically have low antitumor activity, these antibodies are conjugated to effector molecules like cytotoxic agents, immunotoxins such as the bacterial toxin pseudomonas exotoxin A, and radiopharmaceutical agents [4]. Ideally, the antibody-drug conjugate should not be active while circulating through the body, and only have

activity once internalized. This can be controlled with the use of an acid labile linker during the conjugation of the antibody to the drug. Once the antibody-drug conjugate binds to a cancer cell, it can be internalized via receptor mediator endocytosis. In an endosome, which has a pH of roughly 5, the linker is cleaved, and the active version of the drug is released [3], [4], [6]. Despite the promise of this method, initial results were disappointing, with modest cell killing activity, lack of selectivity, and low intracellular drug concentration [3], [7]. In addition, the therapeutic windows are hampered by toxicities related to the drug component of the antibody-drug conjugate [7]. Though there have been efforts to improve the use of antibody-drug conjugates, many challenges still remain for this method of controlled delivery [4].

Another method for specific delivery of cancer therapeutic agents involves taking advantage of the enhanced permeability and retention (EPR) effect [5], [8]–[10]. This EPR effect describes the phenomenon in which macromolecules and small molecules in the 60-400 nm size range extravasate and accumulate in tumors due to the inherent leaky vasculature in cancerous tissues and poor lymphatic drainage [8]. The advantage of this approach is that the potential accumulation of nanosized agents within tumors can enhance therapeutic payloads to the sites of the tumors [9], [10]. Despite this accumulation, several challenges and barriers to this method still remain. Although the permeability and retention of the nanosized agents are enhanced, the improvement is only modest, with only a rough 2-fold increase in delivery compared to normal critical organs [9]. Thus, if the drug stays in circulation for a long time, it can also extravasate into normal tissues, limiting the specificity of this delivery technique. This is partially due to the fact that increased vessel permeability and poor lymphatic drainage also results in high interstitial fluid pressure in solid tumors, which decreases the convection of nanosized drugs into the tumor site [9]. In addition, rapid and unchecked tumor growth results in solid stress vessel compression,

which reduces perfusion. The reduced perfusion limits the distribution of nanosized drugs into the tumor site as well [9]. The combined issues with the EPR effect limits the efficacy of this delivery system, and thus there remains a need to develop an improved method of targeted delivery for cancer cells.

1.2. Disease Detection

1.2.1. Introduction: Chlamydia

Chlamydia is the most common bacterial sexually transmitted infection worldwide [11]. Caused by infections of the bacteria *Chlamydia trachomatis* (*C. trachomatis,* CT), it causes urethritis in men and cervicitis in women [12]. Chlamydia is typically asymptomatic, and thus frequently progresses to complications [13]. Left untreated, the disease can progress to more severe health problems, such as pelvic inflammatory disease and ectopic pregnancies [12].

Currently, chlamydia infections are diagnosed by laboratory testing such as nucleic acid amplification tests [11].Though these types of testing are highly accurate and have a low rate of false positives, they require expensive lab equipment, trained personnel, and are extremely time intensive, resulting in barriers to diagnosis and potential secondary transmissions [11]. There is thus a clinical need for developing a point-of-care (POC) device that is more accessible and rapid.

### 1.2.2. Lateral-Flow Immunoassay (LFA)

An ideal POC device would ideally satisfy the World Health Organization's (WHO's) ASSURED criteria and be affordable, sensitive, specific, user-friendly, rapid and robust, equipment-free, and deliverable to end users [14]. One potential assay that can satisfy some of these criteria is the lateral-flow immunoassay (LFA). The LFA is paper-based, inexpensive, driven

3

by capillary pressure and thus does not require vacuums or pumps, and requires little to no extra training [15].

The LFA detects for the presence or absence of a given biomarker by utilizing colorimetric indicators such as colloidal gold nanoparticles (GNPs) that are conjugated to an antibody specific for that biomarker. A typical LFA has three main components to the test: a sample pad, conjugate pad, detection zone, and absorbent pad (**Fig 1.1a**). The function of the sample application pad is to absorb sample fluid. As the sample fluid wicks up by capillary action, the sample fluid comes in contact with the conjugate pad. The conjugate pad contains dehydrated GNPs, as well as preservation components such as sucrose or trehalose to enhance the longevity of dehydrated biomolecules [16]–[20]. Once the fluid front reaches the end of the conjugate pad, the conjugates are rehydrated, and the solution starts wicking into the middle detection zone. This detection zone is typically constructed of a nitrocellulose membrane material [21], [22].

In the sandwich assay format of the LFA, antibodies against the target biomarker are immobilized on the membrane to constitute a test line. Secondary antibodies or immunoglobulin binding proteins such as Protein A are immobilized upstream to constitute a control line. As the sample fluid containing the target biomarker and the dehydrated GNPs are wicked up into the nitrocellulose detection zone region, biomarker-colloidal GNP complexes present in a positive test sample can bind to the test line due to antibody-binding interactions. This results in the biomarker being "sandwiched" between two antibodies and immobilized on the test line. As the fluid front continues to move, antibodies on the GNPs will interact with secondary antibodies on the control line and become immobilized as well, signifying a valid test. Thus, a positive test is indicated by the presence of two lines on a sandwich format LFA, and a negative test is indicated by the presence of a single line (**Fig 1.2.1b**). Lastly, the fluid is absorbed by the absorbent pad.

4
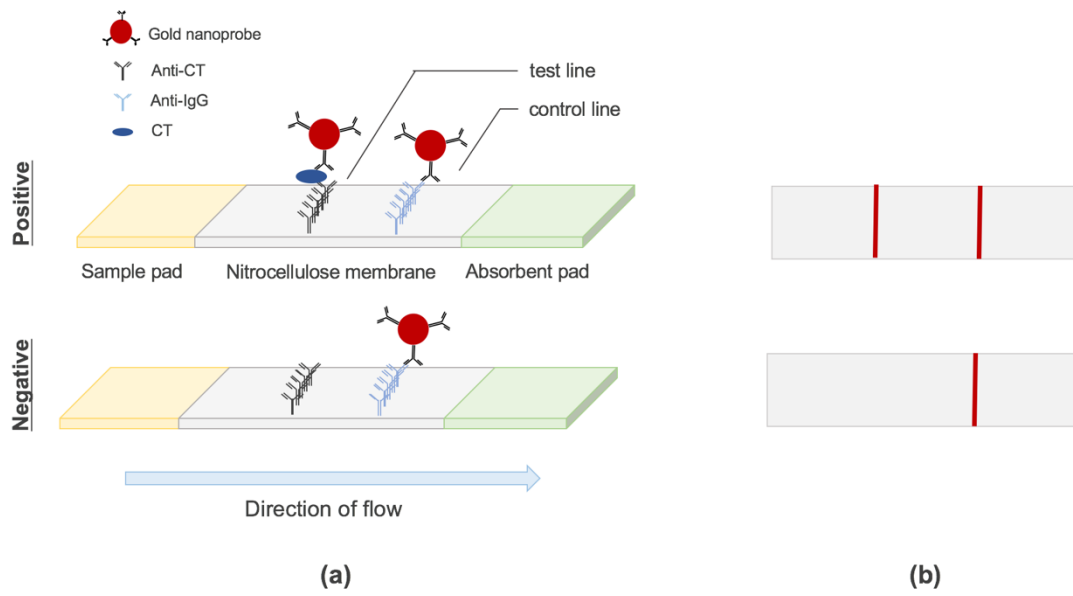
Fig 1.1 Schematic of the LFA sandwich assay. *The setup of the test is shown in (a), and the test results as seen by the user is shown in (b).*

While commercial LFAs for chlamydia detection do exist, they often require a diluent as a component of the assay, which reduces the concentration of the bacteria found to a fraction of its original concentration [11]. The resultant low concentrations decrease the sensitivity of the assay. There thus remains a significant need for LFAs to be improved.

One approach to improving the sensitivity of LFA tests is to enhance the signal to increase the intensity of the signal at the detection zone. Approaches such as enzymatic signal enhancement, silver enhancement, and gold enhancement have been studied in the literature [14], [23]–[27]. However, these types of methodologies require the use of multiple reagents and thus several precisely timed steps, which diminishes the user-friendliness of LFAs and their applicability as POC tests. Controlling fluid flow and precise biomolecule delivery is thus necessary to develop an LFA integrated with signal enhancement technology in an automated, single-step format.

1.2.2. Current Methods of Controlled Delivery for Diagnostic Applications

Developing methods of controlled biomolecule delivery is necessary in order to implement more complex paper-based immunoassays. Discussed below are several attempts from the literature to develop methods of fluidic manipulation.

The first class of controlled delivery methods for paper-based immunoassays requires an additional user step. For example, the Yager group at the University of Washington has previously developed a foldable paper card in which a user step of folding places components of the paper assay in contact with each other and initiates the test [28]. The folding paper card format can also be used during the test to initiate subsequent steps [24]. Another example is the use of a paper-based slip device developed by Kwon and coworkers, in which sequential delivery was achieved by sliding a slip on the device [29]. Though these methods are effective, the use of an additional user step limits the user-friendliness of the test and strays from the WHO's ASSURED criteria.

Another method of controlled delivery for paper-based immunoassays involves manipulation of paper geometric designs. Altering dimensions of the channel such as the length and width of the paper strip can tune the fluid flow speed [30]. In addition, geometric designs of the paper test can be manipulated such that multiple flows are created to deliver reagents [28]. Yet another geometric approach that has been studied involves the slowing of fluid flow with a fluidic shunt. In this method, fluid is diverted into a parallel strip of paper, providing fluidic resistance [31]. Though this approach is relatively simple, it does require the use of more paper and can thus limit the test to only larger volume samples.

Recently, control valves have also been fabricated for paper-based tests. A fluidic diode that promotes or stops wicking along a paper channel was developed by the Faghri group and incorporated into a fluidic circuit [32]. The group achieved flow directionality with the control

valve by fabricating the hydrophilic channel such that only one side surrounding a hydrophobic region had a dehydrated surfactant-rich region. Fluid could then only flow from the surfactant-rich region to the hydrophobic region. Though this approach is effective, this type of fluidic valve mechanism releases many surfactants, which can denature and/or affect the binding ability of the antibodies that are central to paper-based immunoassay technology [33].

Another popular method of controlled delivery is the use of dissolvable barriers to slow down fluid flow. One approach is to dehydrate components such as sucrose onto a paper strip. Fluidic delays can thus be achieved through the increased time required to resolubilize the sucrose. In addition, the viscosity of the solution increases due to the addition of sucrose, and the fluid front travels more slowly in accordance with the Washburn equation [34]. Another type of dissolvable barrier that has been studied utilizes water soluble pullulan films [35]. The method of dissolvable barriers, however, results in the addition of components to the assay, which has the potential to interfere with antibody binding and analyte detection.

2. Development of a Mathematical Model for Controlled Delivery of Mutant Transferrin-CRM107 Molecule Conjugates for Targeted Cancer Therapy

Cancer is the second leading cause of death in the United States, with over 1.6 million new cancer cases and 590,000 deaths in the country every year [36]. Though traditional treatments such as chemotherapy can be effective, they frequently cause dangerous side effects due to nonspecific off-target toxicity. One method to improve targeted drug delivery is through the use of drugs conjugated to transferrin (Tf). Human serum Tf is a monomeric glycoprotein with a molecular weight of approximately 80 kDa, which is involved in transporting iron to the cells in the body. Because of the overexpression of the transferrin receptor (TfR) on a variety of metastatic cells, Tf has been investigated as a potential targeting agent for cancer treatment [2], [37], [38]. Though Tf has been shown to be effective in targeting cancerous cells, its ability to delivery therapeutics is often limited by its inherent TfR-mediated intracellular trafficking pathway. For example, the entire Tf cycle has been shown to last only ~5 min in a human erythroleukemia-derived cell line (K562 cells), and therefore, 30 successive cycles of Tf-toxin conjugate trafficking would be needed before the cytotoxicity on the cell can be observed [39], [40]. Furthermore, after iron-loaded Tf (holo-Tf) delivers its iron payload within the cell, the iron-free Tf (apo-Tf) has significantly reduced binding affinity to TfR outside the cell, and therefore, is unable to re-enter the trafficking pathway until it can bind to free iron, which is not an efficient process [41]–[43]. While the cycle demonstrates evolutionary efficiency for rapidly delivering large quantities of iron to cells, this short duration limits the window of opportunity for Tf to deliver a cytotoxic payload.

To identify a molecular-level design criterion to increase the time Tf spends with the cell (*i.e.,* increase its cellular association) and predict trends, our laboratory previously developed a mathematical model of the Tf/TfR intracellular trafficking pathway based on the principles of mass

action kinetics [44], [45]. Through analysis of the model, our research group discovered that an increase in cellular association could be accomplished by inhibiting the iron delivery rate of Tf. We subsequently demonstrated that two engineered Tf mutants (K206E/R632A Tf and K206E/R534A Tf) with reduced iron release rates dramatically increased cellular association in HeLa and glioma cells. These Tf mutants were then conjugated to DT, and the mutant Tf-DT conjugates were significantly more cytotoxic than the wild-type Tf-DT conjugate when administered to HeLa and glioma cells [46], [47]. Though these mutant Tf conjugates with DT were effective against cancer cells, they cannot be utilized clinically due to the potential of DT to cause toxicity at off-target sites. It has been suggested that only a few micrograms of DT cause death in an unimmunized human [48]. In fact, our previous studies have shown that a conjugate concentration lower than 3.16×10^{-11} M will cause cell death [46]. Thus, an alternative drug to DT must be investigated for clinical treatment.

In this work, we aimed to address this challenge by developing a mathematical model that can predict the behavior of other toxins conjugated to Tf. For this theoretical investigation of a novel conjugate, we chose to study a mutant of DT known as cross-reacting material 107 (CRM107). CRM107 is identical to DT but with two point mutations that decrease its binding affinity to its native receptor, heparin-binding epidermal growth factor precursor (preHB-EGF), by 8,000 fold [49]. The reduction in binding affinity to this DT receptor (DTR) can potentially lower nonspecific toxicity. In addition, unlike other toxins with negligible toxic side effects, *e.g.*, saporin and gelonin, CRM107 maintains the inherent membrane translocation activity of DT, providing CRM107 with a means of endosomal escape upon cellular internalization. By facilitating its localization to the cytosol, its site of action, the efficacy of the toxin following receptor-mediated endocytosis is greatly improved. Thus, CRM107 has the potential for reducing

nonspecific toxicity at off-target sites while maintaining toxicity in tumor cells. Furthermore, our prior experience with DT allows us to translate our mutant Tf-DT conjugate formulation and characterization methods to CRM107.

We modeled the Tf-toxin conjugates by extending our previous Tf/TfR trafficking model to include the DT/DTR trafficking pathway. **Fig. 2.1** shows the transferrin-related trafficking parameters associated with ligand/receptor and ligand/metal interactions that we have previously investigated [45]. Holo-Tf first binds to its receptor on the cell surface at a rate of $k_{FeTf,TfR}$, and is internalized at a rate of $k_{int,Tf}$. The iron can then be released from the transferrin ($k_{Fe,rel}$), and apo-Tf is either degraded ($k_{deg,Tf}$) or recycled to the surface (k_{rec}). To account for DT and its mutant, CRM107, the DT/DTR trafficking pathway (**Fig 2.2**) was investigated. The Tf-DT conjugates can enter via the DT pathway through DT binding to its native receptor (k_{DT}) and being internalized ($k_{int,DT}$). The catalytic domain of DT (DTA) is then separated from its receptor-binding and translocation domains (DTB) and translocated into the cytosol (k_{trans}), where the toxin kills the cell. The DT receptor is then degraded ($k_{deg}(1-f_{DT})$), where f_{DT} is the fraction of internalized DT sorted for translocation. Species balances associated with this combined Tf-DT trafficking model can be found in the Materials and Methods section.
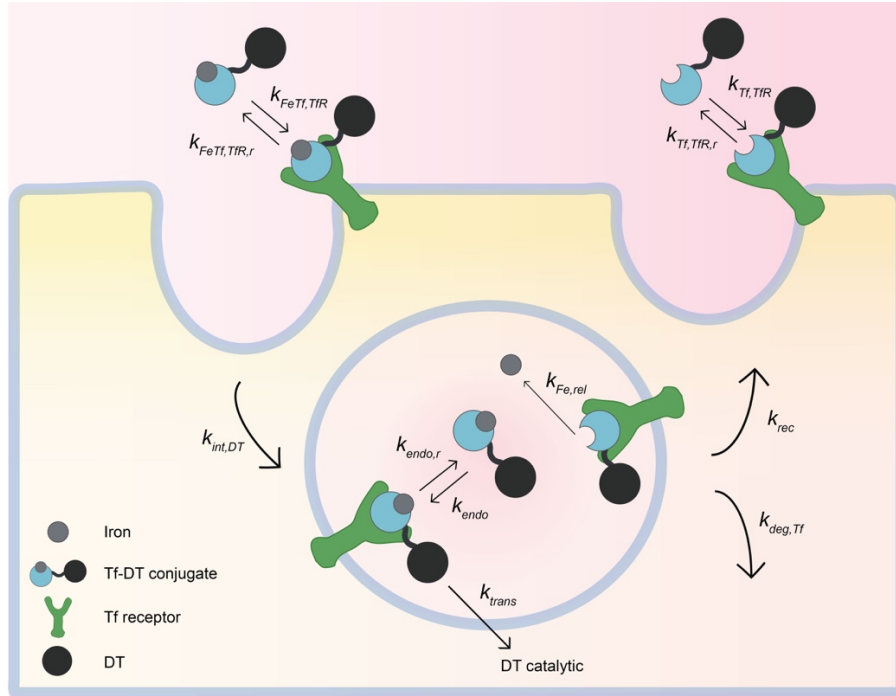
Fig. 2.1 Tf-related trafficking parameters used in the combined Tf-DT trafficking pathway. *For this part of the pathway, holo-Tf conjugated with DT enters the cell through TfR, then internalized as a holo-Tf/TfR complex. DT can then be cleaved, and DTA is released into the cytosol. After iron from Tf is released, the apo-Tf/TfR complex is either degraded or recycled. For the recycled apo-Tf/TfR complex, the apo-Tf is released when it returns to the cell surface.*
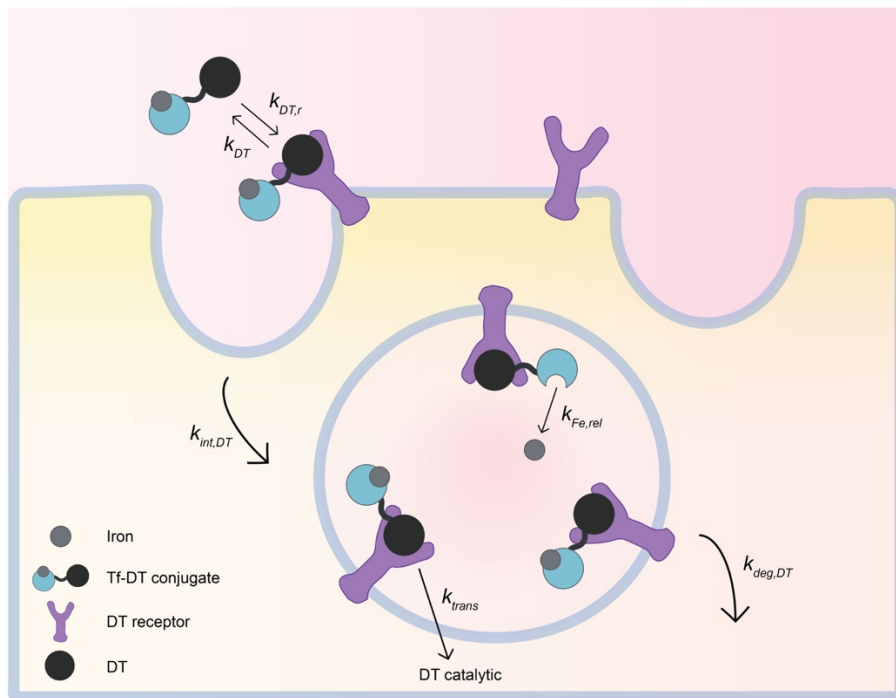
Fig. 2.2 DT-related trafficking parameters used in the combined Tf-DT trafficking pathway. *For this part of the pathway, Tf-DT conjugates enter the cell through binding to DTR. The Tf-DT/DTR complex is then internalized, where*

DT can be cleaved and DTA can be translocated into the cytosol. In addition, once inside the cell, iron can be released from Tf, and the Tf-DT/DTR complex can be degraded.

In this study, we used our mathematical model of the Tf-DT intracellular trafficking pathway to investigate the cytotoxicity of native Tf and our mutant Tf (K206E/R632A Tf and K206E/R534A Tf) conjugated to DT and CRM107. These simulations were performed to theoretically examine the use of mutant Tf as a targeting ligand for CRM107 and investigate the efficacy of those conjugates against cancer cells, as mutant Tf-CRM107 conjugates are assumed to only enter cells through the Tf/TfR trafficking pathway. We also used the mathematical model to investigate whether or not changing the toxin moiety of our Tf-based therapeutic agent to CRM107 actually results in selectivity against normal cells and an improved therapeutic index. These mathematical predictions were then validated using *in vitro* studies in various cancerous and non-cancerous cell lines.

2.2   Materials and Methods

2.2.1   Mathematical model of DT/DTR intracellular trafficking

A DT/DTR intracellular trafficking model was derived using the principles of mass action kinetics and was incorporated into our previous Tf/TfR model. The assumptions for this model are listed below, as are the species balances associated with this extension. Model parameters are discussed in this section as well.

Model Assumptions

The behavior of this model was defined through several assumptions as described below.

i.   The total number of DTR was assumed to be constant, as an equal number of DTR was assumed to be synthesized by the cell as was degraded.

ii.   The DTR is typically processed by one of two ways. It is either proteolytically processed into its mature soluble form, or it is internalized into the cell for degradation [50]. DTR turnover occurs primarily through this latter internalization pathway. The model assumed that the proteolytic processing of DTR is negligible. The model also assumed that the internalization rate was the same for free and DT-bound DTR, since it is believed that DT enters cells by hijacking this inherent internalization pathway of DTR.

iii.   Internalized DTR was assumed to only follow the lysosomal degradation pathway upon clathrin-dependent internalization. This is supported by studies of the effects of protein biosynthesis inhibitors on the DT/DTR trafficking cycle. These studies demonstrate that inhibition of cellular protein biosynthesis prevents the recovery of steady-state levels of cell-surface DTR following internalization. Cell-surface levels of this protein are re-established to steady-state levels upon removal of the inhibitor, suggesting DTR must be constantly re-synthesized [51].

iv.   It was assumed that once the DT/DTR complex is internalized, DT does not dissociate from its receptor.

v.   It was assumed that once the catalytic domain of DT (DTA) is separated from its receptor-binding and translocation domains (DTB) and released into the cytosol, it was not inactivated or degraded within the timeframe of the model simulation. This is supported by experiments demonstrating that more than 80% of DTA directly injected into the cytosol of Ehrlich ascites tumor cells can be recovered intact following a 20 h incubation [52].

Model Equations

Species balances were written for the DT/DTR trafficking pathway based on the model assumptions listed previously. Note that the model accounts for some spatial dependence by defining separate species based on their locations.

Species balance for bulk extracellular DT

$$\frac{d(DT_{bulk})}{dt} = (-k_{DT}DT_{bulk}DTR_{surf} + k_{DT,r}DT\_DTR_{surf})\frac{n_{cell}}{V_{bulk}N_A} \tag{2.1}$$

Species balance for surface DTR

$$\frac{d(DTR_{surf})}{dt} = -k_{int,DT}DTR_{surf} - k_{DT}DT_{bulk}DTR_{surf} + k_{DT,r}DT\_DTR_{surf}$$

$$+ k_{deg}DT\_DTR_{lys} + k_{deg}DTR_{lys} + k_{deg}DTB\_DTR_{lys} \tag{2.2}$$

Species balance for surface DT/DTR complex

$$\frac{d(DT\_DTR_{surf})}{dt} = k_{DT}DT_{bulk}DTR_{surf} - k_{DT,r}DT\_DTR_{surf} - k_{int,DT}DT\_DTR_{surf} \tag{2.3}$$

Species balance for endosomal DTR

$$\frac{d(DTR_{en})}{dt} = k_{int,DT}DTR_{surf} - k_{lys}DTR_{en} \tag{2.4}$$

Species balance for endosomal DT/DTR complex

$$\frac{d(DT\_DTR_{en})}{dt} = k_{int,DT}DT\_DTR_{surf} - k_{trans}f_{DT}DT\_DTR_{en} - k_{lys}(1-f_{DT})DT\_DTR_{en} \tag{2.5}$$

Species balance for endosomal DTB/DTR complex

$$\frac{d(DTB\_DTR_{en})}{dt} = k_{trans}f_{DT}DT\_DTR_{en} - k_{lys}DTB\_DTR_{en} \tag{2.6}$$

Species balance for lysosomal DTR

$$\frac{d(DTR_{lys})}{dt} = k_{lys}DTR_{en} - k_{deg}DTR_{lys} \tag{2.7}$$

Species balance for lysosomal DT/DTR complex

$$\frac{d\left(DT\_DTR_{lys}\right)}{dt} = k_{lys}(1 - f_{DT})DT\_DTR_{en} - k_{deg}DT\_DTR_{lys} \tag{2.8}$$

Species balance for lysosomal DTB/DTR complex

$$\frac{d(DTB\_DTR_{lys})}{dt} = k_{lys}DTB\_DTR_{en} - k_{deg}DTB\_DTR_{lys} \tag{2.9}$$

Species balance for cytosolic DTA

$$\frac{d(DTA_{cyt})}{dt} = k_{trans}f_{DT}DT\_DTR_{en} \tag{2.10}$$

Model Parameters

While $k_{int,DT}$ was estimated directly from empirical data found in the literature, other parameters (*i.e.*, k_{DT}, $k_{DT,r}$, k_{trans}, k_{lys}, k_{deg}) were estimated by fitting our model equations to experimental data found in the literature using least squares minimization. The following paragraphs will discuss how the model parameter values were determined. A full list of model parameters can be found in **Table 2.1**.

The internalization rate constant $k_{int,DT}$ for DTR and the DT/DTR complex was determined from studies performed by Leppla and colleagues on Vero monkey kidney cells [53]. Vero cells are highly sensitive to diphtheria toxin, and have been demonstrated to express between 1 x 10^5 and 2 x 10^5 receptors for DT [54]. Vero cells were pre-bound at 4°C with ^{125}I-labeled DT at a concentration (0.3 µg/mL) that was shown to bind between 1 x 10^4 and 2 x 10^4 surface receptor sites. At this time, the cells were washed to remove any unbound toxin, and the cells were incubated at 37°C in fresh media to initiate cell surface DT/DTR complex internalization. Though some of the receptor-bound DT was found to dissociate from its receptor, this effect was negligible.

These conditions allowed Eq. (2.3) to be simplified to:

$$\frac{d(DT\_DTR_{surf})}{dt} = -k_{int,DT}DT\_DTR_{surf} \qquad (2.11)$$

Equation (2.11) was then integrated. Applying the initial condition that the total number of DT/DTR complexes at t = 0 is DT_DTR$_{surf,0}$ yields:

$$\ln(DT\_DTR_{surf}) = -k_{int,DT}t + \ln(DT\_DTR_{surf,0}) \qquad (2.12)$$

Given the half-time (t = t$_{1/2}$) of DT/DTR complex internalization to be 25 min, where DT_DTR$_{surf}$ is equal to ½ DT_DTR$_{surf,0}$, we estimated $k_{int,DT}$ to be 0.028 min^{-1} [53].

The rate constants k_{DT}, $k_{DT,r}$, k_{trans}, k_{lys}, and k_{deg} were estimated by fitting them using our model equations and the experimental data for cell-mediated DT reduction, as determined by Montecucco and colleagues, using least squares minimization [55]. In this fitting procedure, we first converted the given percentage data to units of molecules/cell. Similar to the Leppla and colleagues study on Vero cell DT internalization, Montecucco and colleagues began their investigation with Vero cells pre-bound with ^{125}I-labeled DT [53]. To attain equilibrium binding, Vero cells were pre-bound with DT by incubating them for 18 h with 3 × 10^{-9} M (DT$_0$) of ^{125}I-labeled DT at 4°C, which inhibits internalization. With this information, we determined the equilibrium number of cell surface DT/DTR complexes (DT_DTR$_{eq}$), in units of molecules/cell, using the following definition of K_D:

$$K_D \equiv \frac{DT_{eq}DTR_{eq}}{DT\_DTR_{eq}} \qquad (2.13)$$

Here, DT$_{eq}$ is the equilibrium molar concentration of unbound DT, DTR$_{eq}$ is the equilibrium number of cell surface receptors in units of molecules/cell, and DT_DTR$_{eq}$ is the equilibrium number of cell surface complexes in units of molecules/cell. Assuming the total number of receptors (DTR$_T$) does not change during this process, we can rewrite DTR$_{eq}$ as:

$$DTR_{eq} = DTR_T - DT\_DTR_{eq} \qquad (2.14)$$

16

Additionally, following appropriate unit conversion, DT_{eq} can be shown to be equal to:

$$DT_{eq} = DT_0 - \frac{DT\_DTR_{eq} n_{cell}}{N_A V_{bulk}} \qquad (2.15)$$

Substituting Eqs. (2.14) and (2.15) into (2.13) and simplifying, we obtain the following expression:

$$\frac{n_{cell}}{N_A V_{bulk}}\left(DT\_DTR_{eq}\right)^2 - \left(K_D + \frac{n_{cell}}{N_A V_{bulk}}(DTR_T) + (DT_0)\right)(DT\_DTR_{eq}) + (DTR_T)(DT_0) = 0$$
$$(2.16)$$

The quadratic equation was used to solve for DT_DTR_{eq}. A DTR_T value of 1.5×10^5 molecules/cell and a DT_0 value of 3×10^{-9} M were used. For n_{cell}, V_{bulk}, and N_A, the values given in **Table 2.1** were used in the solution. With regard to K_D, work by the Mekada laboratory had previously determined its value for the DT/DTR interaction to range from 0.7 to 3×10^{-9} M [56], [57]. As a first approximation for the model, the K_D value of the DT/DTR interaction was estimated to be 10^{-9} M. With these numbers, we evaluated the following:

$$DT\_DTR_{eq} = \begin{cases} 2.57 \times 10^6 \\ or \\ 1.11 \times 10^5 \end{cases} molecules/cell \qquad (2.17)$$

However, since the larger value of DT_DTR_{eq} (2.57×10^6) obtained was greater than DTR_T, this value was clearly not the solution. Therefore, the initial value of DT/DTR complexes on the cell surface in the Montecucco study was estimated as 1.11×10^5 molecules/cell. This initial value of the number of DT/DTR complexes on the cell surface corresponded to approximately the total number of cell-surface DT receptors, which was used to convert the percentage data in the Montecucco study to units of molecules/cell. The conversions were made specifically for the data performed at 37°C investigating the percent ^{125}I-DT released in the medium and associated with cells and the percent ^{125}I-DTA associated with cells. The data was then used to fit the k_{DT}, $k_{DT,r}$, k_{trans}, k_{lys}, and k_{deg} rate constants by using the DT/DTR trafficking model equations and least squares minimization with initial conditions set to zero for all species except DT_DTR_{surf} ($1.11 \times$

10^5 molecules/cell), and DTR$_{surf}$ (3.92×10^4 molecules/cell). The model fit the experimental data

reasonably well. Estimates for the k_{DT}, k_{DTr}, k_{trans}, k_{lys}, and k_{deg} rate constants were determined to

be 1.90×10^7 M^{-1} min^{-1}, 1.90×10^{-2} min^{-1}, 1.5×10^{-1} min^{-1}, 1.8×10^{-1} min^{-1}, and 4.0×10^{-2} min^{-1},

respectively. The fitted parameters k_{DT}, $k_{DT,r}$, k_{lys}, and k_{deg} were reasonably similar to literature

values of comparable biomolecules [58], [59].

With regard to the association rate constant of DT for DTR, k_{DT}, it was estimated by the

following equality for the equilibrium dissociation constant (K_D):

$$K_D = \frac{k_{DT,r}}{k_{DT}} \qquad (2.18)$$

In this estimation, the K_D value of the DT/DTR interaction was again estimated to be 10^{-9} M, and

k_{DTr} was estimated in the above fitting procedure to be 1.90×10^{-2} min^{-1}.

Rate Constant	Definition	Value	Ref.
k_{DT}	Association rate constant of DT for DTR	1.90×10^7 M^{-1} min^{-1}	Est.
$k_{DT,r}$	Dissociation rate constant of DT for DTR	1.90×10^{-2} min^{-1}	Est.
$k_{int,DT}$	Internalization rate constant	2.8×10^{-2} min^{-1}	Est.
k_{trans}	Endosomal translocation rate constant	1.5×10^{-1} min^{-1}	Est.
k_{lys}	Endosome to lysosome rate constant	1.8×10^{-1} min^{-1}	Est.
k_{deg}	Degradation rate constant	4.0×10^{-2} min^{-1}	Est.
f_{DT}	Fraction of internalized DT sorted for translocation	3.33×10^{-1}	(Dorland et al., 1979)
n_{cell}	Cell number	4.75×10^5 cells	(Papini et al., 1993)
V_{bulk}	Bulk media volume	5×10^{-4} L	(Papini et al., 1993)
N_A	Avogadro's number	6.02×10^{23} mol^{-1}	N/A

Table 2.1 List of parameters in the DT/DTR intracellular trafficking model.

2.2.2 Mathematical model of mutant Tf-DT conjugate intracellular trafficking

To fully model the Tf-toxin conjugates, we combined our Tf/TfR model developed previously with the DT/DTR trafficking model developed in Section 2.2.1 [45]. The model assumptions are discussed in this section, as are the relevant equations and parameters.

Model Assumptions

The model assumptions used for the development of the Tf/TfR and DT/DTR (Section 2.2.1) trafficking models also apply to the Tf-DT trafficking model with the following changes and additions [45].

i.   Direct measurements of the iron release rate within cellular endosomes, $k_{Fe,rel}$, are unavailable for both wild-type and mutant Tf. However, since iron is completely released from internalized wild-type Tf prior to recycling back to the cell surface, the same estimate of 100 min^{-1} as used in the Tf/TfR trafficking model was applied to the Tf-DT conjugate trafficking model for wild-type Tf-DT [60].

ii.   Since $k_{Fe,rel}$ for our mutant Tf had previously been estimated to be on the order of 10^{-3} min^{-1}, this value was assumed in the model for mutant Tf-DT conjugates [61].

iii. Since the binding affinity of CRM107 to preHB-EGF is 8,000-fold less than that of DT to preHB-EGF, k_{DT} was lowered by 8,000-fold for CRM107 conjugates.

iv.   The vesicle/tubule partition coefficient, κ, was calculated according to the expression $\kappa = (1-\lambda)^2$, where λ is the diameter of the Tf-DT conjugate divided by the diameter of the tubule [62]. An average Tf-DT conjugate diameter of 20 nm was estimated from the crystal structures of Tf and DT by summing the longest

length scale of each individual molecule together. A tubule diameter of 60 nm was assumed [63]–[65].

v.   Endosomal Tf-DT conjugates, not associated with either receptor, were assumed to be unable to associate with the endosomal membrane and translocate DTA.

vi. It was assumed that the Tf-DT conjugate was required to be associated with TfR in the vesicular compartment (which is destined for degradation) to be competent for DTA translocation into the cytosol when internalized via the Tf/TfR trafficking pathway. This is supported by studies demonstrating that DT membrane insertion and translocation requires an endosomal pH drop to ~4, while endosomal pH is not expected to drop below ~5.5 in the Tf/TfR recycling pathway [40], [66], [67].

vii. It was assumed that once the DT portion of the conjugate had associated with the endosomal membrane and translocated its catalytic domain into the cytosol, the remaining endosomal molecule was sorted for lysosomal degradation through the DT/DTR trafficking pathway irrespective of the receptor the conjugate was associated with.

Model Equations

The full list of all species and parameters, as well as the species balances associated with the Tf-DT conjugate intracellular trafficking model, can be found below. A short description of each species is given prior to each species balance expression. Note that, as before, species are defined based on their type and location in order to recognize the spatial differences in the trafficking pathway. To clarify, any species referred to as "reduced" (*e.g.*, reduced FeTfDT/TfR complex and reduced TfDT/DTR complex) signifies that the disulfide bond between the DTA and

20

DTB domains of DT has been cleaved through the process defined by the rate constant k_{trans}. Therefore, reduced versions of the Tf-DT conjugates (*i.e.*, FeTfDT and TfDT) are represented in the species balances as FeTfDTB and TfDTB. The rate constant, k_{trans}, also captures the process by which DTA translocates into the cytosol following this disulfide reduction.

Species	Definition	Species	Definition
$FeTfDT_{bulk}$	Bulk extracellular iron-bound Tf-DT (FeTfDT)	$TfDT\_TfR_{tub}$	Tubular TfDT/TfR complex
$TfDT_{bulk}$	Bulk extracellular iron-free Tf-DT (TfDT)	$FeTfDT_{deg}$	Degraded FeTfDT
TfR_{surf}	Surface TfR	$TfDT_{deg}$	Degraded TfDT
DTR_{surf}	Surface DTR	TfR_{deg}	Degraded TfR
$FeTfDT\_TfR_{surf}$	Surface FeTfDT/TfR complex	DTR_{deg}	Degraded DTR
$TfDT\_TfR_{surf}$	Surface TfDT/TfR complex	$FeTfDT\_TfR_{deg}$	Degraded FeTfDT/TfR complex
$FeTfDT\_DTR_{surf}$	Surface FeTfDT/DTR complex	$TfDT\_TfR_{deg}$	Degraded TfDT/TfR complex
$TfDT\_DTR_{surf}$	Surface TfDT/DTR complex	$FeTfDTB\_TfR_{deg}$	Degraded reduced FeTfDT/TfR complex
$FeTfDT_{ves}$	Vesicular FeTfDT	$TfDTB\_TfR_{deg}$	Degraded reduced TfDT/TfR complex
$TfDT_{ves}$	Vesicular DT	$FeTfDT\_DTR_{deg}$	Degraded FeTfDT/DTR complex
TfR_{ves}	Vesicular TfR	$TfDT\_DTR_{deg}$	Degraded TfDT/DTR complex
DTR_{ves}	Vesicular DTR	$FeTfDTB\_DTR_{deg}$	Degraded reduced FeTfDT/DTR complex
$FeTfDT\_TfR_{ves}$	Vesicular FeTfDT/TfR complex	$TfDTB\_DTR_{deg}$	Degraded reduced TfDT/DTR complex
$TfDT\_TfR_{ves}$	Vesicular TfDT/TfR complex	$FeTfDT_{rec}$	Recycled FeTfDT
$FeTfDTB\_TfR_{ves}$	Vesicular reduced FeTfDT/TfR complex	$TfDT_{rec}$	Recycled TfDT
$TfDTB\_TfR_{ves}$	Vesicular reduced TfDT/TfR complex	TfR_{rec}	Recycled TfR
$FeTfDT\_DTR_{ves}$	Vesicular FeTfDT/DTR complex	$FeTfDT\_TfR_{rec}$	Recycled FeTfDT/TfR complex
$TfDT\_DTR_{ves}$	Vesicular TfDT/DTR complex	$TfDT\_TfR_{rec}$	Recycled TfDT/TfR complex
$FeTfDTB\_DTR_{ves}$	Vesicular reduced FeTfDT/DTR complex	DTA_{cyt}	Cytosolic DTA
$TfDTB\_DTR_{ves}$	Vesicular reduced TfDT/DTR complex	κ	Vesicular/tubule partition coefficient
TfR_{tub}	Tubular TfR	η	Tubule to vesicle volume ratio
$FeTfDT\_TfR_{tub}$	Tubular FeTfDT/TfR complex	γ	TfR-mediated vesicle to tubule rate constant

Table 2.3 List of species and parameters in the Tf-DT trafficking model.

21

Bulk and Surface Equations

Species balance for bulk extracellular iron-bound Tf-DT (FeTfDT)

$$\frac{d(FeTfDT_{bulk})}{dt} = \left(-k_{FeTf}FeTfDT_{bulk}TfR_{surf} + k_{FeTf,r}FeTfDT\_TfR_{surf} - k_{DT}FeTfDT_{bulk}DTR_{surf}\right.$$

$$\left. + k_{DT,r}FeTfDT\_DTR_{surf} + k_{rec}FeTfDT_{rec}\right)\frac{n_{cell}}{V_{bulk}N_A} \qquad (2.19)$$

Species balance for bulk extracellular iron-free Tf-DT (TfDT)

$$\frac{d(TfDT_{bulk})}{dt} = \left(-k_{Tf}TfDT_{bulk}TfR_{surf} + k_{Tf,r}TfDT\_TfR_{surf} - k_{DT}TfDT_{bulk}DTR_{surf}\right.$$

$$\left. + k_{DT,r}TfDT\_DTR_{surf} + k_{rec}TfDT_{rec}\right)\frac{n_{cell}}{V_{bulk}N_A} \qquad (2.20)$$

Species balance for surface TfR

$$\frac{d(TfR_{surf})}{dt} = -k_{FeTf}FeTfDT_{bulk}TfR_{surf} + k_{FeTf,r}FeTfDT\_TfR_{surf}$$

$$- k_{Tf}TfDT_{bulk}TfR_{surf} + k_{Tf,r}TfDT\_TfR_{surf} - k_{int,Tf}TfR_{surf}$$

$$+ k_{rec}TfR_{rec} + k_{deg,Tf}TfR_{deg} + k_{deg,Tf}FeTfDT\_TfR_{deg}$$

$$+ k_{deg,Tf}TfDT\_TfR_{deg} + k_{deg,DT}FeTfDTB\_TfR_{deg}$$

$$+ k_{deg,DT}TfDTB\_TfR_{deg} \qquad (2.21)$$

Species balance for surface DTR

$$\frac{d(DTR_{surf})}{dt} = -k_{DT}FeTfDT_{bulk}DTR_{surf} + k_{DT,r}FeTfDT\_DTR_{surf} - k_{DT}TfDT_{bulk}DTR_{surf}$$

$$+ k_{DT,r}TfDT\_DTR_{surf} - k_{int,DT}DTR_{surf} + k_{deg,DT}DTR_{deg}$$

$$+ k_{deg,DT}FeTfDT\_DTR_{deg} + k_{deg,DT}TfDT\_DTR_{deg}$$

$$+ k_{deg,DT}FeTfDTB\_DTR_{deg} + k_{deg,DT}TfDTB\_DTR_{deg} \qquad (2.22)$$

Species balance for surface FeTfDT/TfR complex

$$\frac{d(FeTfDT\_TfR_{surf})}{dt}$$

$$= k_{FeTf}FeTfDT_{bulk}TfR_{surf} - k_{FeTf,r}FeTfDT\_TfR_{surf} - k_{int,Tf}FeTfDT\_TfR_{surf}$$

$$+ k_{rec}FeTfDT\_TfR_{rec} \qquad (2.23)$$

22

Species balance for surface TfDT/TfR complex

$$\frac{d\left(TfDT\_TfR_{surf}\right)}{dt}$$

$$= k_{Tf}TfDT_{bulk}TfR_{surf} - k_{Tf,r}TfDT\_TfR_{surf} - k_{int,Tf}TfDT\_TfR_{surf}$$

$$+ k_{rec}TfDT\_TfR_{rec} \tag{2.24}$$

Species balance for surface FeTfDT/DTR complex

$$\frac{d\left(FeTfDT\_DTR_{surf}\right)}{dt} = k_{DT}FeTfDT_{bulk}DTR_{surf} - k_{DT,r}FeTfDT\_DTR_{surf} - k_{int,DT}FeTfDT\_DTR_{surf}$$

$$\tag{2.25}$$

Species balance for surface TfDT/DTR complex

$$\frac{d\left(TfDT\_DTR_{surf}\right)}{dt} = k_{DT}TfDT_{bulk}DTR_{surf} - k_{DT,r}TfDT\_DTR_{surf} - k_{int,DT}TfDT\_DTR_{surf}$$

$$\tag{2.26}$$

Vesicular Equations

Species balance for vesicular FeTfDT

$$\frac{d(FeTfDT_{ves})}{dt} = -k_{Fe,rel}FeTfDT_{ves} - \frac{k_{endo}FeTfDT_{ves}TfR_{ves}}{N_A V_{endo}} + k_{endo,r}FeTfDT\_TfR_{ves}$$

$$- \frac{k_{endo}FeTfDT_{ves}TfR_{tub}}{N_A V_{endo}} + \frac{k_{endo,r}FeTfDT\_TfR_{tub}}{\kappa} - \frac{k_{sv}FeTfDT_{ves}}{1+\eta}$$

$$- \frac{\eta k_{st}FeTfDT_{ves}}{1+\eta} \tag{2.27}$$

Species balance for vesicular TfDT

$$\frac{d(TfDT_{ves})}{dt} = k_{Fe,rel}FeTfDT_{ves} - \frac{k_{endo}TfDT_{ves}TfR_{ves}}{N_A V_{endo}} + k_{endo,r}TfDT\_TfR_{ves}$$

$$- \frac{k_{endo}TfDT_{ves}TfR_{tub}}{N_A V_{endo}} + \frac{k_{endo,r}TfDT\_TfR_{tub}}{\kappa} - \frac{k_{sv}TfDT_{ves}}{1+\eta} - \frac{\eta k_{st}TfDT_{ves}}{1+\eta}$$

$$\tag{2.28}$$

Species balance for vesicular TfR

$$\frac{d(TfR_{ves})}{dt} = k_{int,Tf}TfR_{surf} - \frac{k_{endo}FeTf\ DT_{ves}TfR_{ves}}{N_AV_{endo}} + k_{endo,r}FeTfDT\_TfR_{ves}$$

$$- \frac{k_{endo}TfDT_{ves}TfR_{ves}}{N_AV_{endo}} + k_{endo,r}TfDT\_TfR_{ves} - \gamma TfR_{ves} - k_{sv}TfR_{ves}$$

$$(2.29)$$

Species balance for vesicular DTR

$$\frac{d(DTR_{ves})}{dt} = k_{int,DT}DTR_{surf} - k_{lys}DTR_{ves} \qquad (2.30)$$

Species balance for vesicular FeTfDT/TfR complex

$$\frac{d(FeTfDT\_TfR_{ves})}{dt}$$

$$= k_{int,Tf}FeTfDT\_TfR_{surf} - k_{Fe,rel}FeTfDT\_TfR_{ves} + \frac{k_{endo}FeTfDT_{ves}TfR_{ves}}{N_AV_{endo}}$$

$$- k_{endo,r}FeTfDT\_TfR_{ves} - k_{trans}FeTfDT\_TfR_{ves} - \gamma FeTfDT\_TfR_{ves}$$

$$- k_{sv}FeTfDT\_TfR_{ves} \qquad (2.31)$$

Species balance for vesicular TfDT/TfR complex

$$\frac{d(TfDT\_TfR_{ves})}{dt}$$

$$= k_{int,Tf}TfDT\_TfR_{surf} + k_{Fe,rel}\ FeTfDT\_TfR_{ves} + \frac{k_{endo}TfDT_{ves}TfR_{ves}}{N_AV_{endo}}$$

$$- k_{endo,r}TfDT\_TfR_{ves} - k_{trans}TfDT\_TfR_{ves} - \gamma TfDT\_DTR_{ves} - k_{sv}TfDT\_TfR_{ves}$$

$$(2.32)$$

Species balance for vesicular reduced FeTfDT/TfR complex

$$\frac{d(FeTfDTB\_TfR_{ves})}{dt} = k_{trans}FeTfDT\_TfR_{ves} - k_{Fe,rel}FeTfDTB\_TfR_{ves} - k_{lys}FeTfDTB\_TfR_{ves}$$

$$(2.33)$$

Species balance for vesicular reduced TfDT/TfR complex

$$\frac{d(TfDTB\_TfR_{ves})}{dt} = k_{trans}TfDT\_TfR_{ves} + k_{Fe,rel}FeTfDTB\_TfR_{ves} - k_{lys}TfDTB\_TfR_{ves}$$

(2.34)

Species balance for vesicular FeTfDT/DTR complex

$$\frac{d(FeTfDT\_DTR_{ves})}{dt}$$

$$= k_{int,DT}FeTfDT\_DTR_{surf} - k_{Fe,rel}FeTfDT\_DTR_{ves} - k_{trans}f_{DT}FeTfDT\_DTR_{ves}$$

$$- k_{lys}(1 - f_{DT})FeTfDT\_DTR_{ves}$$

(2.35)

Species balance for vesicular TfDT/DTR complex

$$\frac{d(TfDT\_DTR_{ves})}{dt}$$

$$= k_{int,DT}TfDT\_DTR_{surf} + k_{Fe,rel}FeTfDT\_DTR_{ves} - k_{trans}f_{DT}TfDT\_DTR_{ves}$$

$$- k_{lys}(1 - f_{DT})TfDT\_DTR_{ves}$$

(2.36)

Species balance for vesicular reduced FeTfDT/DTR complex

$$\frac{d(FeTfDTB\_DTR_{ves})}{dt}$$

$$= k_{trans}f_{DT}FeTfDT\_DTR_{ves} - k_{Fe,rel}FeTfDTB\_DTR_{ves} - k_{lys}FeTfDTB\_DTR_{ves}$$

(2.37)

Species balance for vesicular reduced TfDT/DTR complex

$$\frac{d(TfDTB\_DTR_{ves})}{dt} = k_{trans}f_{DT}TfDT\_DTR_{ves} + k_{Fe,rel}FeTfDTB\_DTR_{ves} - k_{lys}TfDTB\_DTR_{ves}$$

(2.38)

Tubular Equations

Species balance for tubular TfR

$$\frac{d(TfR_{tub})}{dt} = -\frac{\kappa k_{endo} FeTfDT_{ves} TfR_{tub}}{N_A V_{endo}} + k_{endo,r} FeTfDT\_TfR_{tub} - \frac{\kappa k_{endo} TfDT_{ves} TfR_{tub}}{N_A V_{endo}}$$

$$+ k_{endo,r} TfDT\_TfR_{tub} + \gamma TfR_{ves}$$

(2.39)

Species balance for tubular FeTfDT/TfR complex

$$\frac{d(FeTfDT\_TfR_{tub})}{dt}$$

$$= -k_{Fe,rel} FeTfDT\_TfR_{tub} + \frac{\kappa k_{endo} FeTfDT_{ves}}{N_A V_{endo}} - k_{endo,r} FeTfDT\_TfR_{tub}$$

$$+ \gamma FeTfDT\_TfR_{ves} - k_{st} FeTfDT\_TfR_{tub}$$

(2.40)

Species balance for tubular TfDT/TfR complex

$$\frac{d(TfDT\_TfR_{tub})}{dt}$$

$$= k_{Fe,rel} FeTfDT\_TfR_{tub} + \frac{\kappa k_{endo} TfDT_{ves} TfR_{tub}}{N_A V_{endo}} - k_{endo,r} TfDT\_TfR_{tub}$$

$$+ \gamma TfDT\_TfR_{ves} - k_{st} TfDT\_TfR_{tub}$$

(2.41)

Degradation Equations

Species balance for degraded FeTfDT

$$\frac{d(FeTfDT_{deg})}{dt} = \frac{k_{sv} FeTfDT_{ves}}{1 + \eta} - k_{deg,Tf} FeTfDT_{deg}$$

(2.42)

Species balance for degraded TfDT

$$\frac{d(TfDT_{deg})}{dt} = \frac{k_{sv} TfDT_{ves}}{1 + \eta} - k_{deg,Tf} TfDT_{deg}$$

(2.43)

Species balance for degraded TfR

$$\frac{d(TfR_{deg})}{dt} = k_{sv} TfR_{ves} - k_{deg,Tf} TfR_{deg}$$

(2.44)

Species balance for degraded DTR

$$\frac{d(DTR_{deg})}{dt} = k_{lys}DTR_{ves} - k_{deg,DT}DTR_{deg} \tag{2.45}$$

Species balance for degraded FeTfDT/TfR complex

$$\frac{d(FeTfDT\_TfR_{deg})}{dt} = k_{sv}FeTfDT\_TfR_{ves} - k_{deg,Tf}FeTfDT\_TfR_{deg} \tag{2.46}$$

Species balance for degraded TfDT/TfR complex

$$\frac{d(TfDT\_TfR_{deg})}{dt} = k_{sv}TfDT\_TfR_{ves} - k_{deg,Tf}TfDT\_TfR_{deg} \tag{2.47}$$

Species balance for degraded reduced FeTfDT/TfR complex

$$\frac{d(FeTfDTB\_TfR_{deg})}{dt} = k_{lys}FeTfDTB\_TfR_{ves} - k_{deg,DT}FeTfDTB\_TfR_{deg} \tag{2.48}$$

Species balance for degraded reduced TfDT/TfR complex

$$\frac{d(TfDTB\_TfR_{deg})}{dt} = k_{lys}TfDTB\_TfR_{ves} - k_{deg,DT}TfDTB\_TfR_{deg} \tag{2.49}$$

Species balance for degraded FeTfDT/DTR complex

$$\frac{d(FeTfDT\_DTR_{deg})}{dt} = k_{lys}(1 - f_{DT})FeTfDT\_DTR_{ves} - k_{deg,DT}FeTfDT\_DTR_{deg}$$
$$\tag{2.50}$$

Species balance for degraded TfDT/DTR complex

$$\frac{d(TfDT\_DTR_{deg})}{dt} = k_{lys}(1 - f_{DT})TfDT\_DTR_{ves} - k_{deg,DT}TfDT\_DTR_{deg}$$
$$\tag{2.51}$$

Species balance for degraded reduced FeTfDT/DTR complex

$$\frac{d(FeTfDTB\_DTR_{deg})}{dt} = k_{lys}FeTfDTB\_DTR_{ves} - k_{deg,DT}FeTfDTB\_DTR_{deg}$$
$$\tag{2.52}$$

Species balance for degraded reduced TfDT/DTR complex

$$\frac{d(TfDTB\_DTR_{deg})}{dt} = k_{lys}TfDTB\_DTR_{ves} - k_{deg,DT}TfDTB\_DTR_{deg}$$

27

$$\tag{2.53}$$

Recycling Equations

Species balance for recycled FeTfDT

$$\frac{d(FeTfDT_{rec})}{dt} = \frac{\eta \kappa k_{st} FeTfDT_{ves}}{1 + \eta} - k_{rec} FeTfDT_{rec}$$

(2.54)

Species balance for recycled TfDT

$$\frac{d(TfDT_{rec})}{dt} = \frac{\eta \kappa k_{st} TfDT_{ves}}{1 + \eta} - k_{rec} TfDT_{rec}$$

(2.55)

Species balance for recycled TfR

$$\frac{d(TfR_{rec})}{dt} = k_{st} TfR_{tub} - k_{rec} TfR_{rec}$$

(2.56)

Species balance for recycled FeTfDT/TfR complex

$$\frac{d(FeTfDT\_TfR_{rec})}{dt} = k_{st} FeTfDT\_TfR_{tub} - k_{rec} FeTfDT\_TfR_{rec}$$

(2.57)

Species balance for recycled TfDT/TfR complex

$$\frac{d(TfDT\_TfR_{rec})}{dt} = k_{st} TfDT\_TfR_{tub} - k_{rec} TfDT\_TfR_{rec}$$

(2.58)

Cytosolic Equations

Species balance for cytosolic DTA

$$\frac{d(DTA_{cyt})}{dt} = k_{trans} FeTfDT\_TfR_{ves} + k_{trans} TfDT\_TfR_{ves} + k_{trans} f_{DT} FeTfDT\_DTR_{ves} + k_{trans} f_{DT} TfDT\_DTR_{ves}$$

(2.59)

Model Parameters

Mutant Tf conjugates were differentiated from wild-type Tf conjugates by altering the iron release rate within cellular endosomes, $k_{Fe,rel}$, such that mutant Tf conjugates had a lower $k_{Fe,rel}$. CRM107 conjugates were differentiated from DT conjugates by altering the binding affinity to DTR. CRM107's decreased binding affinity for DTR was modeled by setting the DT to DTR

association rate constant, k_{DT}, of Tf-CRM107 simulations to be 8,000-fold less than its value for Tf-DT simulations. Note that this same distinction between Tf-DT and Tf-CRM107 conjugates can also be accomplished by increasing the DT to DTR dissociation rate constant, $k_{DT,r}$, by 8,000-fold for Tf-CRM107 simulations since $K_D = k_{DT\ r}/k_{DT}$. It was found with the cellular toxicity simulations that either method produced the same outcome. The results in Section 3 correspond to decreasing the association rate constant for Tf-CRM107 conjugates. In addition, the same rate constant for TfR-mediated internalization was assumed for both Tf and its mutant. This was deduced from the fact that the TfR-mediated internalization rate constant remains the same regardless of whether there is Tf bound to TfR, which suggests that the internalization rate constant would not depend on the type of Tf bound to TfR [68]. A full list of model parameters is provided in **Table 2.2**.

Rate Constant	Definition	Value	Ref.
k_{FeTf}	Association rate constant of FeTfDT for TfR	$(9.6 \pm 0.2) \times 10^7$ M^{-1} min^{-1}	(Lebron et al., 1998)
$k_{FeTf,r}$	Dissociation rate constant of FeTfDT for TfR	$(7.8 \pm 1.2) \times 10^{-2}$ min^{-1}	(Lebron et al., 1998)
k_{Tf}	Association rate constant of TfDT for TfR	0 M^{-1} min^{-1}	(Lebron et al., 1998)
$k_{Tf,r}$	Dissociation rate constant of TfDT for TfR	2.6 min^{-1}	(Ciechanover et al., 1983)
k_{DT}	Association rate constant of (Fe)TfDT for DTR	1.90×10^7 M^{-1} min^{-1} [a] 2.375×10^3 M^{-1} min^{-1} [b]	Est.
$k_{DT,r}$	Dissociation rate constant of (Fe)TfDT for DTR	1.90×10^{-2} min^{-1}	Est.
k_{endo}	Endosomal association rate constant of (Fe)TfDT for TfR	$(4.4 \pm 0.4) \times 10^7$ M^{-1} min^{-1}	(Lebron et al., 1998)
$k_{endo,r}$	Endosomal dissociation rate constant of (Fe)TfDT for TfR	$(5.6 \pm 1.2) \times 10^{-2}$ min^{-1}	(Lebron et al., 1998)
$k_{int,Tf}$	TfR-mediated internalization rate constant	2.0×10^{-1} min^{-1}	(Ciechanover et al., 1983)
$k_{int,DT}$	DTR-mediated internalization rate constant	2.8×10^{-2} min^{-1}	(Dorland et al., 1979)
$k_{Fe,rel}$	Endosomal Tf iron release rate constant	1.0×10^2 min^{-1} [c] 1.0×10^{-3} min^{-1} [d]	Est.
k_{trans}	Vesicle to cytosol translocation rate constant	1.5×10^{-1} min^{-1}	Est.
k_{sv}	TfR-mediated degradation rate constant	1.2×10^{-1} min^{-1}	(French and Lauffenburger, 1997)
k_{st}	TfR-mediated tubule to recycling rate constant	5.3×10^{-1} min^{-1}	(French and Lauffenburger, 1997)
$k_{deg,Tf}$	TfR-mediated degradation rate constant	6.0×10^{-2} min^{-1}	(French and Lauffenburger, 1997)
k_{rec}	TfR-mediated recycling rate constant	1.5×10^{-1} min^{-1}	(French and Lauffenburger, 1997)
κ	Vesicle/tubule partition coefficient	0.44	Est.
η	Tubule to vesicle volume ratio	0.43	(French and Lauffenburger, 1997)
γ	TfR-mediated vesicle to tubule rate constant	1.0 min^{-1}	(French and Lauffenburger, 1997)
k_{lys}	DTR-mediated vesicle to lysosome transfer rate constant	1.8×10^{-1} min^{-1}	Est.
$k_{deg,DT}$	DTR-mediated degradation rate constant	4.0×10^{-2} min^{-1}	Est.
f_{DT}	Endosome to cytosol translocation fraction	0.33	(Dorland et al, 1979)
n_{cell}	Cell number	4×10^5 cells	N/A
V_{bulk}	Bulk media volume	1×10^{-3} L	N/A
V_{endo}	Endosomal volume	1.0×10^{-14} L	(French and Lauffenburger, 1997)
N_A	Avogadro's number	6.02×10^{23} mol^{-1}	N/A

[a] Wild-type DT
[b] CRM107
[c] Wild-type Tf
[d] Mutant Tf

Table 2.2 List of parameters in the Tf-DT conjugate intracellular trafficking model.

2.2.3 Synthesis and Purification

Synthesis and Purification of CRM107

CRM107 was first developed by Laird and Groman and purified as described previously by Youle and coworkers [39], [69]. Briefly, *Corynebacterium diphtheria* cultures were clarified by centrifugation, incubated in 65% ammonium sulfate at 4°C overnight, and subsequently centrifuged and resuspended in 50 mM tris(hydroxymethyl)aminomethane (Tris) buffer with 0.1 mM ethylenediaminetetraacetic acid (EDTA) at pH 8.0. The solution was then dialyzed overnight at 4°C in the same buffer with 0.1 mM phenylmethylsulfonyl fluoride added. CRM107 was isolated by ion-exchange chromatography using a DEAE-Sepharose Fast Flow column (GE Healthcare Life Sciences, Marlborough, MA).

Synthesis and Purification of Tf Mutants

The generation of Tf mutants with site-directed mutagenesis was previously described. [61], [70], [71]. The mutant Tf expression vectors were pNUT N-His K206E/K534A hTf NG and pNUT NHis K206E/R632A hTf NG, which coded for two Tf mutants with changes to both iron binding lobes. Furthermore, pNUT N-His hTf NG expression vector (native Tf) was also created to serve as the control for the two Tf mutants. The production and purification of the recombinant Tf was previously described [70], [71]. Briefly, baby hamster kidney cells were used for the expression of secreted recombinant Tf, and the protein was subsequently purified from the cell culture medium.

2.2.4 Cell Culture

U251 human glioma cells were a kind gift from Drs. Robert M. Prins and Linda M. Liau (UCLA Neurosurgery). Normal human astrocytes (NHAs) were purchased from Lonza (Rockland, ME). U87 human glioma cells, human umbilical vein endothelial cells (HUVECs), and HeLa cells were purchased from American Type Culture Collection (ATCC). All cells were seeded on 75 cm^2 culture flasks (Corning, Corning, NY) for everyday passaging. U251, U87, and HeLa cells were grown in Dulbecco's Modified Eagle Medium supplemented with high glucose (DMEM-HG; Invitrogen, Carlsbad, CA) with 3.6 g/L sodium bicarbonate, 10% fetal bovine serum (FBS; Hyclone, Logan, UT), 1 mM sodium pyruvate, 100 units/mL penicillin (Invitrogen), and 100 µg/mL streptomycin (Invitrogen) at a pH of 7.4. HUVECs were grown in Ham's F12 Medium with Kaighn's Modification (F12K) with 2.5 g/L sodium bicarbonate, 10% FBS, 0.1 mg/mL porcine heparin, 0.03 mg/mL endothelial cell growth supplement, 1 mM sodium pyruvate, 100 units/mL penicillin (Invitrogen), and 100 µg/mL streptomycin (Invitrogen) at a pH of 7.4. NHAs were grown in Astrocyte Growth Medium (AGM; Lonza). All cell culture media described above will be referred to as growth media. The cells were incubated in a humidified atmosphere with 5% CO_2 at 37°C. All reagents and materials were purchased from Sigma-Aldrich (St. Louis, MO) unless otherwise specified.

2.2.5 Conjugation of Recombinant Tf to CRM107

CRM107 conjugates of recombinant Tf were prepared using the chemical crosslinkers 2-iminothiolane (IT; Pierce, Rockford, IL) and N-succinimidyl 3-(2-pyridyldithio)propionate (SPDP; Pierce) to create a reducible disulfide bond. CRM107 in borate buffer (100 mM sodium borate, 3.5 mM EDTA, pH 8.0) was thiolated with a 2.0-fold molar excess of 2-IT for 60 min at

32

room temperature. The thiolated CRM107 was separated from free 2-IT using Zeba desalting spin columns (Pierce). Recombinant Tf in phosphate-buffered saline (PBS; 50 mM sodium phosphate, 0.15 M NaCl, pH 7.4) was reacted with a 3.0-fold molar excess of SPDP for 30 min at room temperature. This SPDP modified Tf (Tf-SPDP) was separated from free SPDP using Zeba desalting spin columns. The Tf-SPDP and the thiolated CRM107 (1:1 molar ratio) were mixed, diluted, and incubated for 20 h at 4°C. The Tf-CRM107 conjugate was then purified by HPLC (AKTA FPLC Chromatographic System, GE Healthcare Bio-Sciences, Piscataway, NJ) using two HiPrep 16/60 Sephacryl S200HR size-exclusion columns in series (GE Healthcare Bio-Sciences). The identity of each peak was confirmed by SDS-PAGE and the concentration quantified using the Bradford dye binding assay (Bradford, 1976). The Tf-CRM107 conjugate was stored in PBS containing 20 mM sodium bicarbonate.

2.2.6   *In Silico* Cytotoxicity

Cellular Toxicity in Cancerous Cells

Model equations were solved with Berkeley Madonna™ using initial conditions set to zero for all species except the concentration of holo-Tf-DT (1 nM), the number of TfR on the cell surface (5.4×10^5 receptors [43]), and the number of DTR on the cell surface (1.5×10^5 receptors [54]). The length of each simulation was 50 h. Wild-type Tf conjugates were distinguished from mutant Tf conjugates by setting the endosomal iron release rate constant, $k_{Fe,rel}$, to 100 min^{-1} and 0.001 min^{-1}, respectively. Tf-CRM107 conjugate trafficking was distinguished from Tf-DT conjugate trafficking by reducing the association rate constant for toxin binding to DTR (k_{DT}) to be 8,000-fold less.

Cellular toxicity was investigated by examining the % inhibition of cellular growth at various concentrations of the Tf-toxin conjugate. Tf-toxin conjugate-induced cellular toxicity was estimated using the following approach. First, based on our previous Tf-DT conjugate *in vitro* toxicity studies with U251 and U87 cells, maximum wild-type Tf-DT toxicity initially plateaued at a conjugate concentration of 3.16×10^{-11} M for both cell lines [46]. The number of molecules of DT's catalytic domain (DTA) found in the cytosol at this concentration was determined from trafficking simulations to be 1.51×10^4 molecules/cell, and this was fixed as the number of DTA molecules necessary to exhibit 100% cellular toxicity for our model simulations. Lower concentrations of conjugates were also input into the trafficking model to generate a cytotoxicity curve. After determining the number of DTA molecules in the cytosol, the value was divided by 1.51×10^4 and multiplied by 100% to yield the corresponding % inhibition value.

Cellular Toxicity in Non-Neoplastic Cells

Cellular toxicity for non-neoplastic cells was investigated similarly to the procedure outlined in Section 2.3.1, with the exception of the initial value of surface Tf receptors. Since cancerous cells are known to overexpress surface TfR, non-neoplastic cells were modeled by decreasing the initial surface TfR of cancerous cells, 5.4×10^5 receptors, by various fold [2], [43]. Since non-neoplastic cells were expected to have at least 10-fold fewer TfR than cancerous cells, this investigation was started at a 10-fold decrease of TfR.

2.2.7 *In Vitro* Cytotoxicity

Tf-toxin conjugates were synthesized and various cell lines were cultured according to methods detailed previously. The sulforhodamine B (SRB) cell proliferation assay was used to

quantify cell survival based on the measurement of cellular protein content. The toxicities of the mutant Tf-CRM107 conjugates relative to the wild-type Tf-CRM107 conjugate were investigated in glioma cells (U87 and U251) and HeLa cells to determine if the mutant Tf conjugates were more potent than the wild-type Tf conjugate using the new toxin. In addition, mutant Tf-CRM107 conjugates were incubated with normal cells to assess cancer specificity.

The various cells utilized in this study were seeded onto wells of a 96-well tissue culture plate at cell densities of 10,000 cells/cm^2 for cancer cells (U87, U251, and HeLa) and 45,000 cells/cm^2 for normal cells (human umbilical vein endothelial cell (HUVEC) and normal human astrocyte (NHA)). Different seeding densities were used due to differences in cell size and proliferation rate. Following overnight incubation, growth medium was aspirated, and the cells were incubated for 48 h with 100 µL fresh growth medium containing concentrations of Tf-CRM107 spanning five orders of magnitude (10^{-13} to 10^{-9} M). A cold 10% trichloroacetic acid (TCA) solution (100 µL) was added to each well to fix the cells at 4°C for 1 h. The 10% TCA solution was removed, and the cells were washed four times with deionized water then thoroughly blow-dried. Subsequently, 50 µL of a 1% acetic acid solution containing 0.4% SRB was added to each well for 30 min at room temperature. The dye solution was removed, and the cells were washed four times with a 1% acetic acid solution to remove unbound dye; following this step, the cells were again blow-dried. The dye was dissociated from the proteins and solubilized with 100 µL of a 10 mM Tris base solution. The absorbance of each well was determined with an Infinite F200 plate reader (Tecan System Inc., San Jose, CA) at wavelengths of 560 and 700 nm. The survival of cells relative to a control (*i.e.,* cells incubated in growth medium without Tf-CRM107) was calculated by determining the ratio of the (A_{560} - A_{700}) values. Experiments were performed three times with quadruplicate points per concentration.

2.3   Results and Discussion

2.3.1 Sensitivity Analysis of the Parameters Associated with the DT/DTR Intracellular Trafficking Pathway

All parameters associated with the DTR-mediated internalization pathway were examined to investigate the effects of this alternative internalization pathway on the overall cellular toxicity between wild-type and mutant Tf-DT conjugates. Tf-CRM107 conjugates were largely ignored in these analyses since the effect of varying these DT related parameters on a conjugate with an 8,000-fold decreased binding affinity for DTR produced negligible changes, as illustrated for two such parameters in **Fig 2.3**.
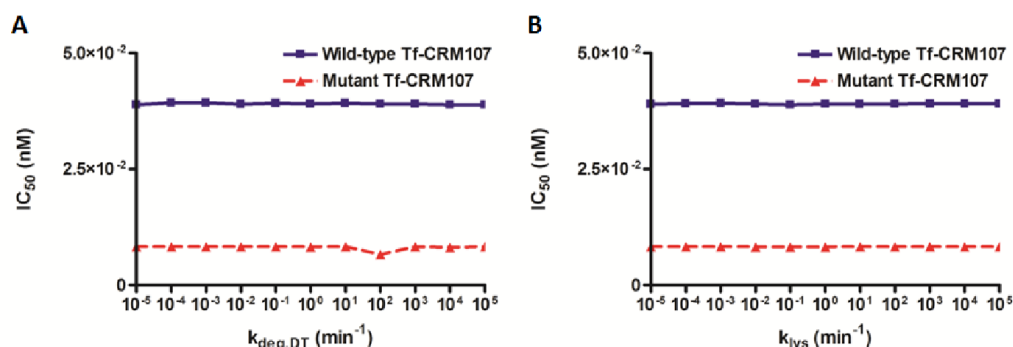
Fig 2.3 Predicted response in cellular toxicity to changes in the (A) degradation and (B) lysosomal sorting rate constants of Tf-CRM107 conjugates internalized through the DT receptor.

The effect of cell surface DTR expression on the cellular toxicity of wild-type and mutant Tf-DT conjugates were examined (**Fig 2.4A**). As the expression of cell surface DTR increased, the cellular toxicity of wild-type Tf-DT conjugates drastically increased, as indicated by decreasing IC$_{50}$ values, with a maximum toxicity observed at an expression level of 10^6 receptors/cell. Beyond this point, the cytotoxic efficacy of wild-type Tf-DT conjugates slightly decreased. This suggests a balance between an increase in cytotoxic efficacy due to the increasing availability of DTR-mediated endocytic entry sites and a decrease in efficacy due to the increasing lysosomal

36

degradation of wild-type Tf-DT conjugates through DTR-mediated endocytosis. Similarly, this decrease is also observed for mutant Tf-DT conjugates at an expression level beyond 10^6 receptors/cell. However, the initial increase in the number of cell surface DTR has a negligible effect on the cytotoxic efficacy of mutant Tf-DT conjugates. This observation supports the hypothesis that the improved cellular association of mutant Tf is sufficient for optimal delivery of toxin, whether it be DT or CRM107. The same trend in toxicity is observed for the sensitivity analysis of k_{DT} and $k_{DT,r}$ (**Figs 2.4B** and **C**) since altering the binding affinity of DT for its receptor has the similar effect as altering cell surface DTR expression.
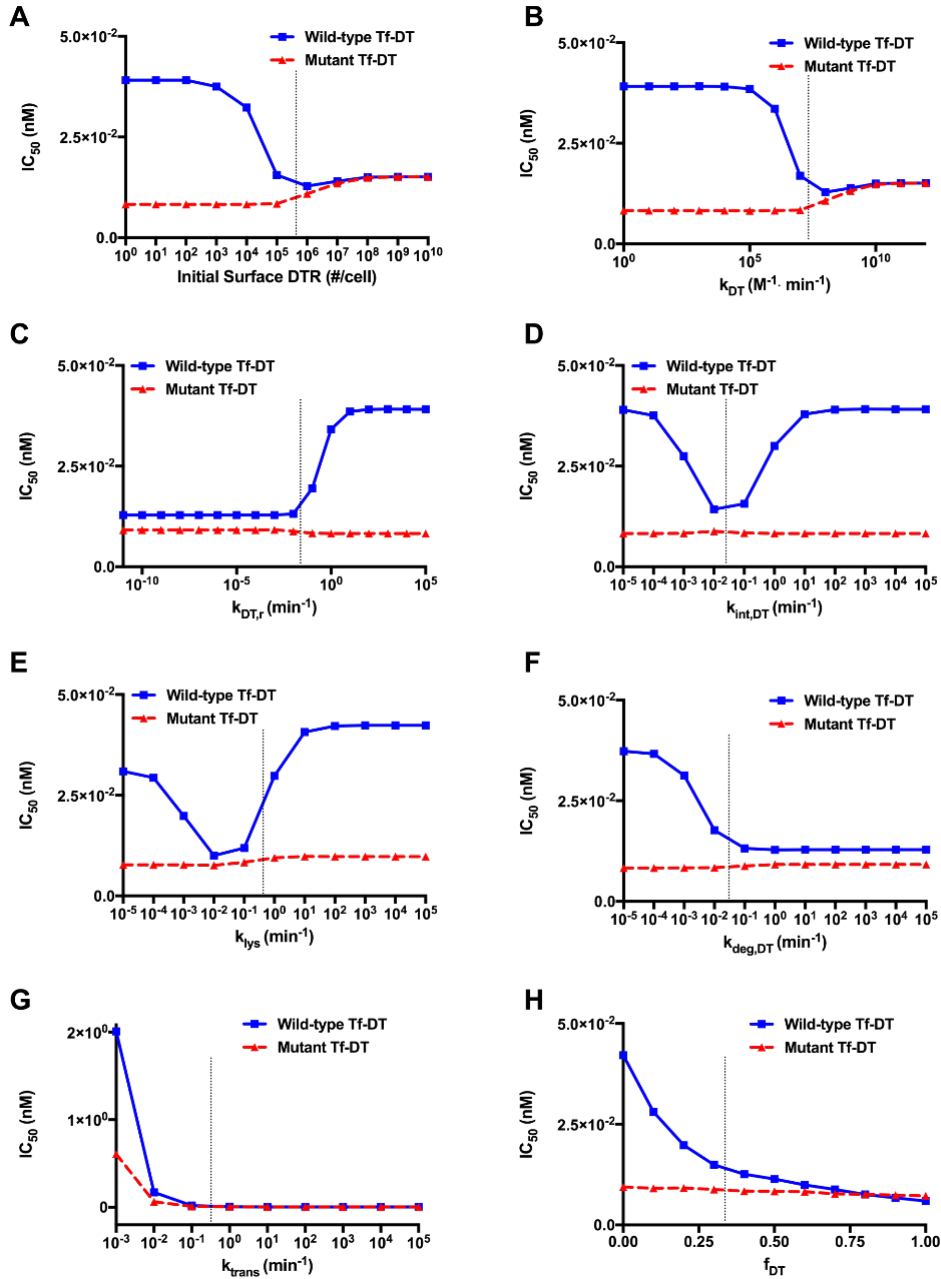
Fig 2.4 Predicted response in cellular toxicity to changes in DT parameters. *Dashed lines indicate native DT values for each property. Note change in y-axis scale for (G).*

The one difference with the analysis of $k_{DT,r}$ is that there is no observable local minimum for the Tf-DT conjugate IC_{50} curve (**Fig 2.4C**). This is unique to the dissociation rate constant since the dissociation of DT from DTR is not possible until the conjugate binds to its receptor. At

this junction, the conjugate can either dissociate from its receptor, or become internalized. The lack of an IC_{50} minimum is attributed to the fact that as you decrease $k_{DT,r}$ to a value lower than the native internalization rate constant of DT, $k_{int,DT}$ (0.028 min^{-1}), the internalization process dominates, leading to no further changes in IC_{50}.

Analyses of $k_{int,DT}$ and k_{lys} (**Figs 2.4D** and **E**) demonstrated similar profiles as those observed for the analyses of cell surface DTR expression and k_{DT}. Initially, increasing both rate constants increased the cytotoxic efficacy of wild-type Tf-DT conjugates, but the efficacy of wild-type Tf-DT conjugates began to decrease beyond values of 10^{-2} min^{-1}. This behavior, with respect to $k_{int,DT}$, occurs since increasing the rate of wild-type Tf-DT conjugate internalization will initially enhance delivery of DT to the cytosol and improve cytotoxicity. However, since DTR can become internalized without first binding to the conjugate, higher internalization rates can lead to a rapid decrease in cell surface DTR expression with localization in the endosome, resulting in the observed decrease in cytotoxic efficacy. In terms of k_{lys}, while the initial increase also facilitates the DTR-mediated delivery of the wild-type Tf-DT conjugate, higher lysosomal sorting rates limit the residence time of these conjugates within the endosome. Since the translocation of DTA occurs at the pre-lysosomal endosome, this shorter endosomal residence time negatively impacts the conjugate's cytotoxic efficacy.

Increasing the degradation rate constant, $k_{deg,DT}$, exhibits an increase in wild-type Tf-DT conjugate cytotoxic efficacy (**Fig 2.4F**), which plateaus at a value of 10^{-1} min^{-1}. This observation is not surprising due to the model assumption that the total number of DTR remains at steady-state. For this reason, as the degradation rate of proteins in the DTR-mediated intracellular trafficking pathway increases, more free receptors are returned to the cell surface, allowing more wild-type Tf-DT conjugates to enter the cell.

Increasing the endosome to cytosol translocation fraction, f_{DT}, and the endosome to cytosol translocation rate constant, k_{trans}, leads to an increase in cytotoxic efficacy for wild-type Tf-DT conjugates, as expected (**Figs 2.4G and H**). This is because an increase in both of these parameters leads to an increased delivery of DTA to the cytosol, improving its cytotoxic efficacy.

Finally, it is important to note that the cytotoxic efficacy of mutant Tf-DT conjugates is only negligibly affected by changes to all DT parameters, with the exception of k_{trans}. This is likely due to the fact that the improved cellular association of mutant Tf is sufficient for optimal delivery of toxin despite alterations to the DTR-mediated trafficking pathway, as discussed previously. The exception found with k_{trans} is ascribed to its contribution to DTA translocation in both DTR- and TfR-mediated intracellular trafficking pathways.

2.3.1   Tf-DT Mathematical Model Successfully Predicts Improved Efficacy of Mutant Tf-CRM107 Conjugates against Cancer Cells Relative to Wild-Type Tf-CRM107 Conjugates

Simulations with our Tf-DT conjugate intracellular trafficking model were performed to determine differences in cytotoxicity between wild-type and mutant Tf proteins with both DT and CRM107 conjugates. The predicted trends were then validated with *in vitro* cytotoxicity data.

Fig 2.5 and **Table 2.3** presents the results of our *in silico* toxicity simulations. The concentrations at which 50% inhibition of cellular growth (IC_{50}) was observed were 13.4, 8.66, 36.8, and 8.20 pM for wild-type Tf-DT, mutant Tf-DT, wild-type Tf-CRM107, and mutant Tf-CRM107, respectively (**Table 2.3**). These results indicate that mutant Tf conjugates have increased drug efficacy compared to the wild-type conjugates. In addition, the difference in drug delivery efficacy between wild-type and mutant Tf was only 1.5-fold for DT conjugates, while the difference for CRM107 conjugates was 4.5-fold. This suggests that changing the toxin moiety of

our Tf-based cancer therapeutic from DT to CRM107 can potentially increase the difference in drug efficacy.
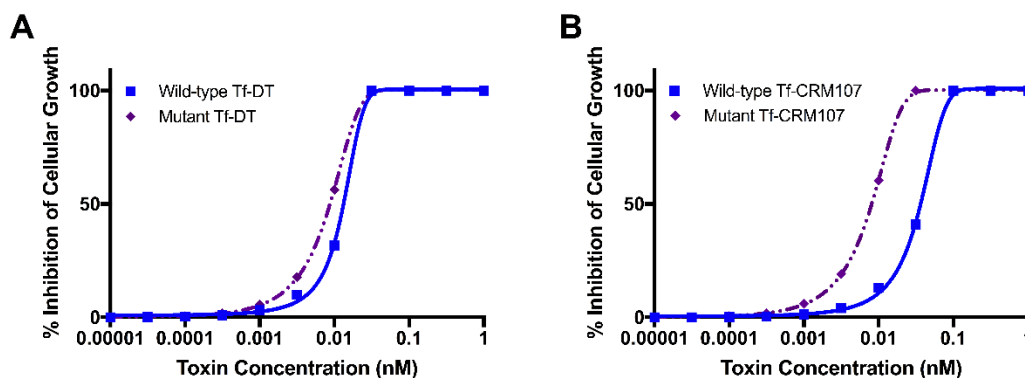
Fig 2.5 Cytotoxicity simulation of wild-type Tf versus mutant Tf conjugates. *In silico cytotoxicity simulations using the Tf-DT mathematical model for (A) wild-type and mutant Tf-DT conjugates and (B) wild-type and mutant Tf-CRM107 conjugates.*

Conjugate	IC$_{50}$ (pM)	IC$_{50}$ decrease associated with mutant Tf
DT conjugates		
Wild-type Tf-DT	13.4	
Mutant Tf-DT	8.66	1.5-fold
CRM107 conjugates		
Wild-type Tf-CRM107	36.8	
Mutant Tf-CRM107	8.20	4.5-fold

Table 2.3 Simulation IC$_{50}$ values of DT conjugates versus CRM107 conjugates. *Mutant Tf conjugates exhibit improved efficacy compared to their wild-type Tf counterparts. Changing the toxin moiety to CRM107 results in an improved fold difference between the mutant Tf and the wild-type Tf conjugates.*

The difference in cytotoxicity between CRM107 and DT was as predicted because the wild-type Tf-CRM107 conjugate was estimated to be associated to a lesser degree with the cell than the wild-type Tf-DT conjugate, since CRM107 cannot bind to DTR (the preHB-EGF receptor). Wild-type Tf is often assumed to be restricted to a single cycle through its trafficking

41

pathway due to its highly efficient iron delivery kinetics [43], [60]. For this reason, wild-type Tf-CRM107 conjugates would typically have a single opportunity to deliver their cytotoxic payload, which is insufficient for the effective delivery of CRM107 given the short intracellular residence time of a single Tf/TfR trafficking cycle [72]. On the other hand, wild-type Tf-DT conjugates are given an additional opportunity to deliver their cytotoxic payload even after the loss of iron because of DT's high affinity for its own receptor. Coupled with the greater intracellular residence time associated with the DT/DTR degradation pathway, it is not surprising that the cytotoxicity of wild-type Tf-DT conjugates is significantly greater than the cytotoxicity of wild-type Tf-CRM107 conjugates [53].

To confirm these trends predicted by the Tf-DT conjugate intracellular trafficking and toxicity model, we synthesized and administered CRM107 conjugates of our wild-type, K206E/R632A, and K206E/K534A Tf ligands to two glioma (U251 and U87) cell lines as well as the HeLa cell line over a range of concentrations for 48 h. In accordance with our model, each mutant Tf-CRM107 conjugate exhibited a significantly enhanced drug delivery efficacy relative to their wild-type counterpart in U87, U251, and HeLa cells that was much greater than the improved efficacy observed with Tf-DT conjugates (**Fig 2.6**, **Table 2.4**). IC_{50} values for U87 cells (**Figs 2.6A** and **B**, **Table 2.4**) were determined to be 32.1 ± 3.2 pM for wild-type Tf compared to values of 7.10 ± 0.87 ($p = 0.0002$) and 6.80 ± 0.52 pM ($p = 0.0002$) for K206E/R632A Tf and K206E/K534A Tf, respectively. Similar results were obtained with U251 cells (**Figs 2.6C** and **D**, **Table 2.4**), demonstrating IC_{50} values of 35.3 ± 3.7 pM for wild-type Tf compared to values of 10.8 ± 1.8 ($p = 0.0005$) and 11.3 ± 1.2 pM ($p = 0.0004$) for K206E/R632A Tf and K206E/K534A Tf, respectively. For HeLa cells (**Figs 2.6E** and **F**, **Table 2.4**), the IC_{50} values were determined to be 30.3 ± 3.0 pM for wild-type Tf compared to values of 9.4 ± 1.0 ($p = 0.0002$) and 10.2 ± 1.4 pM

42

($p = 0.0003$) for K206E/R632A Tf and K206E/K534A Tf, respectively. The student's t-test was used to show that the decrease in IC_{50} exhibited by both mutant Tf-CRM107 conjugates compared to the wild-type counterpart was statistically significant ($p < 0.05$). These experiments showed that mutant Tf-CRM107 conjugates exhibited an improved efficacy compared to wild-type Tf-CRM107 conjugates (4.6, 3.2, and 3.0 fold for U87, U251, and HeLa cells). The fold improvement observed with the mutant Tf-CRM107 conjugates relative to the wild-type Tf-CRM107 conjugate was greater than the fold improvement observed with the mutant Tf-DT conjugates relative to the wild-type Tf-DT conjugate [46], [47].
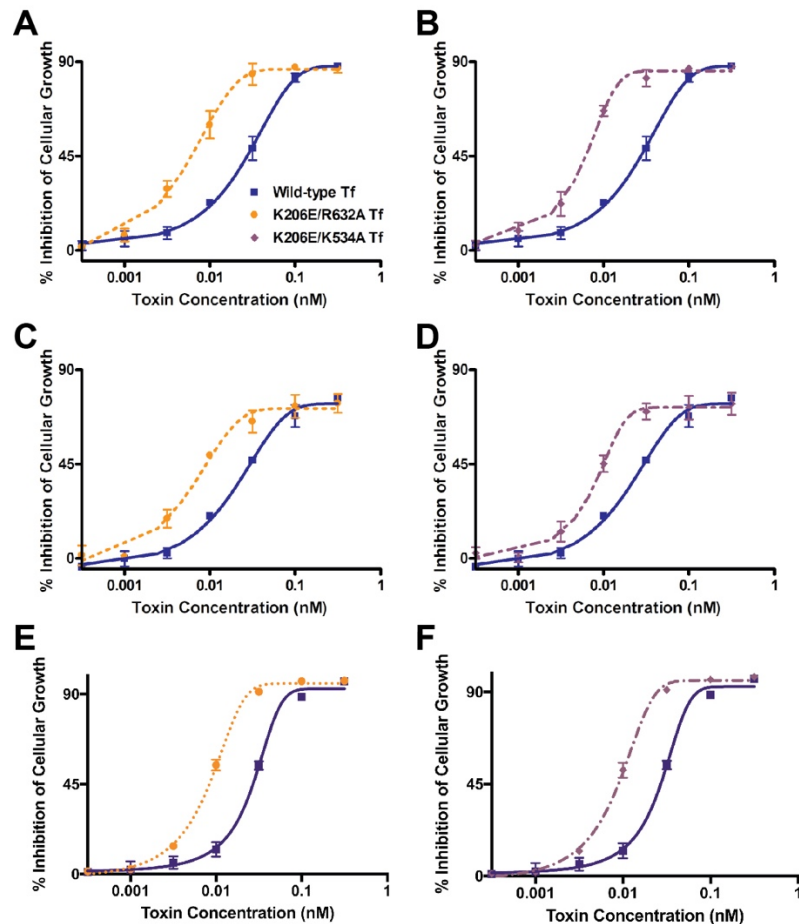
Fig 2.6 *In vitro* cytotoxicity comparisons for CRM107 conjugates. *Points, mean from an average of three experiments; bars, standard deviation. Wild-type Tf versus K206E/R632A Tf and K206E/R534A Tf in (A, B) U87, (C, D) U251, and (E, F) HeLa cells.*

Cell Line	IC$_{50}$ ± SD (pM)	Average IC$_{50}$ decrease associated with mutant Tf
U87		
Wild-type Tf-CRM107	32.1 ± 3.2	
K206E/R632A Tf-CRM107	7.10 ± 0.87	~4.6 fold
K206E/K534A Tf-CRM107	6.80 ± 0.52	
U251		
Wild-type Tf-CRM107	35.3 ± 3.7	
K206E/R632A Tf-CRM107	10.9 ± 1.8	~3.2 fold
K206E/K534A Tf-CRM107	11.3 ± 1.2	
HeLa		
Wild-type Tf-CRM107	30.3 ± 3.0	
K206E/R632A Tf-CRM107	9.4 ± 1.0	~3.0 fold
K206E/K534A Tf-CRM107	10.2 ± 1.4	

Table 2.4 IC$_{50}$ values of various Tf-CRM107 conjugates in cancerous cell lines. *The IC$_{50}$ values of Tf-CRM107 conjugates are listed for U87, U251, and HeLa cells. SD, standard deviation. Mutant Tf-CRM107 conjugates exhibit improved efficacy compared to wild-type Tf-CRM107 conjugates.*

These *in vitro* results are consistent with our projected trends that mutant Tf conjugates have an improved efficacy compared to wild-type Tf conjugates. Our mathematical model of the Tf-DT intracellular trafficking pathway thus successfully predicted that (i) mutant Tf-toxin conjugates were more effective than wild-type Tf-toxin conjugates, and (ii) the increase in drug carrier efficacy for CRM107 conjugates was better than for DT conjugates. These results suggest that CRM107 appears to be a more suitable therapeutic agent for our mutant Tf to deliver to cancer cells.

2.3.2 Tf-DT Mathematical Model Successfully Predicts Selectivity of Mutant Tf-CRM107 for Cancerous Cells Relative to Non-Neoplastic Cells

Simulations with our Tf-DT conjugate intracellular trafficking model were performed to determine differences in selectivity of the mutant Tf-CRM107 conjugate for cancerous, or neoplastic, cells relative to non-neoplastic cells. The predicted trends were then validated with *in vitro* cytotoxicity data.

To simulate the cancer selectivity of our mutant Tf-CRM107 conjugates, we also ran cellular toxicity simulations with varying numbers of TfR receptors. Since TfR is overexpressed on malignant cells at 5.4×10^5 receptors on the cell surface, we varied the number of initial TfR receptors over a range of decreased values to model non-neoplastic cells [2], [43]. The results can be found below in **Fig 2.7**. The simulated IC_{50} values of mutant Tf-CRM107 in neoplastic cells was 8.20 pM, while the simulated values for non-neoplastic cells were 11.5 pM, 16.4 pM, 81.0 pM, and 144.4 pM for 5.4×10^4, 2.97×10^4, 5.4×10^3, and 2.97×10^3 TfR, respectively (**Table 2.5**). The results from this *in silico* study shows the trend that decreasing numbers of TfR (*i.e.*, modeling non-neoplastic cells) results in reduced cytotoxicity of our mutant Tf-CRM107 conjugates. Our model thus predicts that mutant Tf-CRM107 conjugates demonstrate selectivity for cancerous cells relative to non-neoplastic cells, and suggests that they could be used as a targeted cancer therapeutic agent.
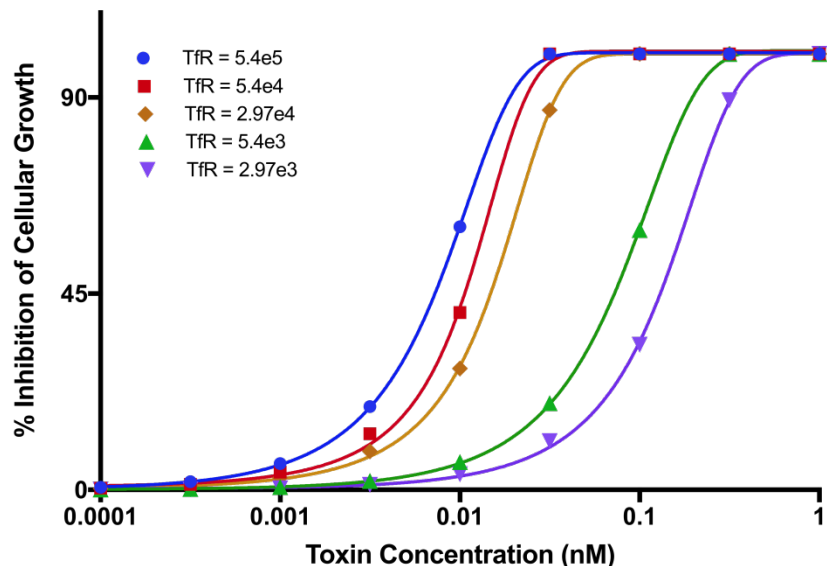
Fig 2.7 Cytotoxicity simulation of mutant Tf-CRM107 conjugates against neoplastic and non-neoplastic cells. *Cytotoxicity curves of neoplastic cells (TfR = 5.4 × 10^4) versus non-neoplastic cells show a trend of reduced cytotoxicity with reduced TfR.*

TfR Number	IC$_{50}$ (pM)
Neoplastic cells	
5.4 × 10^5	8.20
Non-neoplastic cells	
5.4 × 10^4	11.5
2.97 × 10^4	16.4
5.4 × 10^3	81.0
2.97 × 10^3	144.4

Table 2.5 Simulation IC$_{50}$ values of mutant Tf-CRM107 conjugates in neoplastic versus non-neoplastic cells. *Results demonstrate that a decreased number of TfR results in an increased IC$_{50}$ value and reduced cytotoxicity.*

These differences between cancerous and non-neoplastic cells were predicted for mutant Tf-CRM107 because the conjugates are estimated to associate to a lesser degree with cells that have fewer TfR on the surface. Since the binding affinity of CRM107 for DTR is 8,000-fold lower than native values and the binding affinity of mutant Tf to TfR remains the same compared to native values, the main contribution to internalization of the mutant Tf-CRM107 conjugates is the

Tf/TfR pathway [47]. The decreased numbers of TfR on cell surfaces of non-neoplastic cells thus results in decreased mutant Tf-CRM107 internalization. Because of this difference in conjugate internalization for neoplastic versus non-neoplastic cells, the conjugates were less cytotoxic toward and selective against non-neoplastic cells.

To validate our cytotoxicity simulations of the mutant Tf-CRM107 conjugates in non-neoplastic cells, *in vitro* cytotoxicity experiments were performed with two non-neoplastic cell types, HUVECs and NHAs. Our results indicated that cancer selectivity can be achieved by our CRM107 conjugates due to significantly higher IC_{50} values observed for all conjugates when treating non-neoplastic cells, suggesting a potentially good therapeutic index. As seen in **Figs 2.8A and B**, IC_{50} values for HUVECs were determined to be 195 ± 30, 147 ± 36 ($p = 0.2$), and 136 ± 24 pM ($p = 0.06$) for wild-type Tf, K206E/R632A Tf, and K206E/K534A Tf, respectively. Similar results were obtained with NHAs (**Figures 2.8C and D**), demonstrating IC_{50} values of 55.0 ± 9.3, 32.4 ± 7.4 ($p = 0.03$), and 38.0 ± 6.8 pM ($p = 0.06$) for wild-type Tf, K206E/R632A Tf, and K206E/K534A Tf, respectively. Compared to the *in vitro* IC_{50} values for cancerous cells presented in Section 3.1, these values are much higher, confirming our mathematical prediction that our mutant Tf-CRM107 conjugates exhibit selectivity for cancerous cells relative to non-neoplastic cells. From these results, we can conclude that changing the toxin moiety from DT to CRM107, which has an 8,000-fold reduced binding affinity, has a significant contribution to improving the selectivity.
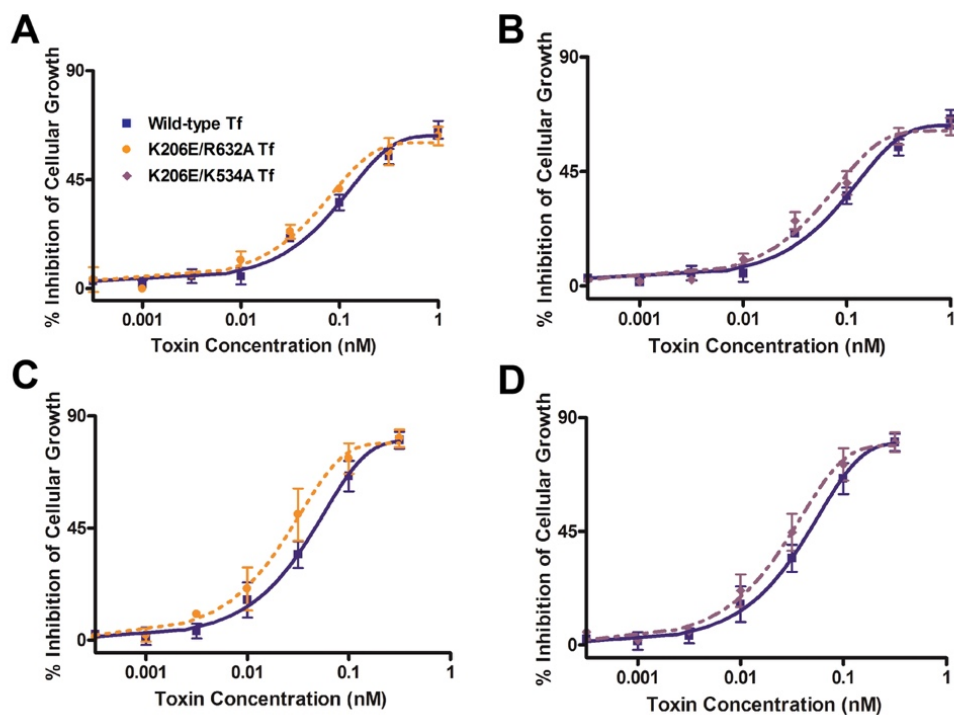
Fig 2.8 *In vitro* cytotoxicity comparisons for CRM107 conjugates for non-neoplastic cells. Points, mean from an average of three experiments; bars, standard deviation. Wild-type Tf versus K206E/R632A Tf and K206E/R534A Tf in (A, B) HUVECs and (C, D) NHAs.

Cell Line	$IC_{50} \pm SD$ (pM)
HUVEC	
Wild-type Tf-CRM107	195 ± 30
K206E/R632A Tf-CRM107	147 ± 36
K206E/K534A Tf-CRM107	136 ± 24
NHA	
Wild-type Tf-CRM107	55.0 ± 9.3
K206E/R632A Tf-CRM107	32.4 ± 7.4
K206E/K534A Tf-CRM107	38.0 ± 6.8

Table 2.6 *In vitro* IC_{50} values of Tf-CRM107 conjugates with non-neoplastic cells. The IC_{50} values for mutant CRM107 against non-neoplastic cells are much higher than against neoplastic cell lines, suggesting a good therapeutic index.

In addition, differences in toxicity between wild-type Tf-CRM107 conjugates and both

mutant Tf-CRM107 conjugates were significantly diminished in non-neoplastic cell lines. The

student's *t*-test was used to show that the decrease in IC$_{50}$ exhibited by both mutant Tf-CRM107 conjugates compared to the wild-type counterpart was not statistically significant ($p > 0.05$), with the exception of the K206E/R632A Tf-CRM107 conjugate against NHAs. The diminished difference in IC$_{50}$ values was likely due to saturation of TfR with the conjugates. Since normal cells are expected to express far fewer TfR, additional recycling capabilities of the mutant conjugates become inconsequential in the presence of excess Tf-CRM107 conjugates available to bind to the receptors and be internalized.

2.4   Conclusion

Due to the overexpression of TfR on cancer cells, targeted cancer therapeutics that exploit the Tf trafficking pathway is currently being evaluated. Previously, we have used a mathematical model of the Tf/TfR pathway to predict that conjugates made with a mutated form of Tf results in improved efficacy in cancer cell lines. Though we have previously investigated mutant Tf-DT conjugates with success, DT has high toxicity and may exhibit dangerous off-target effects.

In this work, we proposed the utilization of a mathematical model to evaluate the efficacy and selectivity of mutant Tf conjugated to an alternate drug. For this mathematical investigation of a novel conjugate, we chose to investigate CRM107, a mutant form of DT. We first extended our previously developed Tf/TfR model to include a DT/DTR pathway. We then used our mathematical model to evaluate how mutant Tf would improve efficacy compared to wild-type Tf when the toxin moiety is changed to CRM107 and whether a mutant Tf-CRM107 conjugate would exhibit improved selectivity against non-neoplastic cells while maintaining cytotoxic efficacy toward cancerous cells.

Through our simulations, we predicted that mutant Tf-CRM107 would outperform wild-type Tf-CRM107 in terms of efficacy toward cancer cells. We also predicted that switching from wild-type Tf to mutant Tf in CRM107 conjugates would drastically improve the efficacy of these conjugates due to the absence of the DT/DTR trafficking pathway for CRM107. In addition, this increase was predicted to be much greater than the increase associated with switching from wild-type Tf to mutant Tf in DT conjugates. This predicted trend was confirmed in our *in vitro* investigation of toxicity with the U87 and U251 glioma cell lines, as well as the HeLa cell line.

We also ran simulations to evaluate the selectivity of this novel mutant Tf-CRM107 conjugate. The results of our simulation suggested that the cytotoxicity of mutant Tf-CRM107 was greater in cancerous cells due to overexpression of TfR on those cells. This predicted trend was confirmed, as our measured *in vitro* IC_{50} values of CRM107 conjugates with normal cell lines were many fold higher than the IC_{50} values observed with cancerous cell lines. Both our *in silico* simulations and *in vitro* results suggest a potentially greater therapeutic window for the mutant Tf-CRM107 conjugates. Furthermore, for the normal cell types (HUVECs and NHAs), the cytotoxicity curves of the mutant and wild-type Tf-CRM107 conjugates became similar, attributed to the saturation of TfR on the normal cells.

In summary, our mathematical model predicted that (i) mutant Tf-CRM107 exhibited improved efficacy compared to wild-type Tf-CRM107, (ii) this improvement in efficacy was greater than that of its DT counterparts, and (iii) mutant Tf-CRM107 exhibits a substantial decrease in toxic side effects. These mathematical simulations, which were validated by our *in vitro* studies, altogether indicate that CRM107 would be a more suitable therapeutic agent in combination with the mutant Tf in future studies.

3. Investigation of Aqueous Two-Phase Systems (ATPSs) and Development of a Housing for Automated Enzymatic Signal Enhancement in Paper-Based Immunoassays

3.1   Introduction

3.1.1   Motivation and background

Chlamydia is the most common bacterial sexually transmitted infection worldwide [11]. Infection of the bacteria *Chlamydia trachomatis* (*C. trachomatis*, CT) causes urethritis in men and cervithritis in women [12]. Though easily treated, the infection is largely underdiagnosed, as it is asymptomatic for 25% of men and up to 80% of women [13]. In addition, when left untreated, the infection can progress to serious health problems such as pelvic inflammatory disease and ectopic pregnancy in women [12]. Though tests such as nucleic acid amplification tests can detect CT with high sensitivity, they require a long turnaround time, causing potential secondary transmissions to occur during this period [11]. Accordingly, there remains a need to develop a rapid and sensitive point-of-care (POC) test.

The lateral-flow immunoassay (LFA) is an inexpensive and rapid paper-based diagnostic assay that has the potential to meet the World Health Organization's ASSURED criteria for POC testing [14]. However, despite the many advantages of using LFA over conventional tests, their commercial sensitivities remain low [11]. One approach to improving the sensitivity of these tests is to enhance the signal and increase the intensity of the signal at the detection zone. Methodologies such as enzymatic signal enhancement, silver enhancement, and gold enhancement have been studied in the literature [14], [23]–[27]. Fluidic manipulations and controlled delivery of multistep assays are thus greatly desired for LFAs to seamlessly integrate these complex systems into the LFA, but their fabrication still remain a challenge [24], [28], [29].

Previously, our research group has investigated controlled delivery of biomolecules in paper-based assays through the novel use of an aqueous two-phase system (ATPS). ATPSs are advantageous for use in an LFA device because they are low-cost, require little extra training, and also provide a mild environment for biomolecules. Our laboratory has previously demonstrated that ATPSs can be used to improve paper-based immunoassays in two ways. Firstly, our group has shown the use of ATPSs to pre-concentrate target biomarkers prior to detection on the LFA and improve sensitivity. The sensitivity of LFA can be improved by 10-fold by pre-concentrating the target biomarkers to a particular phase and applying the concentrated phase to the LFA [73], [74]. Secondly, our laboratory has shown the use of ATPSs to deliver only the concentrated portion to the detection zone by modulating its macroscopic phase separation behavior on paper. Our research group has shown that a homogeneous, well-mixed solution containing the ATPS solution will phase separate rapidly as it wicks up a paper matrix [22], [75]. By changing the 3D architecture of the paper matrix, our lab has shown tunable macroscopic phase separation behavior, such as significantly lowering the phase separation time of an ATPS, and changing the length of the leading phase [22], [75]. By modulating these factors, our research group has been able to demonstrate controlled delivery of biomolecules for the improvement of LFA sensitivity.

This thesis presents more advanced control of biomolecule delivery in paper-based immunoassays and improvement of LFA sensitivity. In this work, we demonstrate (i) the use of an ATPS for as an automated, sequential delivery mechanism for signal enhancement reagents, and (ii) the development of a casing to achieve consistent flow and conjugate release for this system. To our knowledge, this is the first time an ATPS has been used for automated delivery of multiple reagents on paper, and the first time a casing has been used to fine-tune ATPS flow on LFA.

Though there have been attempts to integrate enzymatic signal enhancement techniques in

LFA, previous methodologies have been limited and required the use of multiple user steps to prevent premature enzymatic signal enhancement. Here, we have circumvented this problem by utilizing an ATPS in which an enzyme, conjugated to gold nanoprobes, partition into a phase opposite from its substrates. The ATPS used was the polymer-salt system formed by poly(ethylene glycol-*ran*-propylene glycol) (EOPO) and sodium sulfate salt, and the model enzyme-substrate system chosen was alkaline phosphatase (ALP) and its substrates nitroblue tetrazolium 5-bromo-4-chloro-3-idolyphosphate (NBT/BCIP).

Here, we applied a mixed solution containing ATPS components, CT, gold nanoparticles decorated with ALP and antibodies to *C. trachomatis* (anti-CT-ALP-GNPs), and NBT/BCIP to an LFA test. As the ATPS phase separated through the paper matrix, it first delivered the leading phase containing the concentrated biomarker and anti-CT-ALP-GNPs. Then, as the second phase containing the enzymatic substrates flowed up through the detection zone, ALP that had been immobilized on the test line cleaved the substrate and deposited a purple precipitate, thus enhancing the signal of the paper-based immunoassay.

In addition to controlling the delivery time of two different reagents and allowing for automated sequential delivery, we have demonstrated fine tuning of fluid flow through the paper strip and conjugate release through the development of an acrylic housing. This housing (i) fully enclosed the paper test strip to prevent flow inconsistencies from fluctuating humidity and evaporation and (ii) provided an optimal amount of pressure on the conjugate pad and sample pad wick for sufficient contact and improved fluid flow. The acrylic housing was inexpensive and the manufacturing process was facile, which kept the test cost-effective and deliverable to end users while improving the performance of the test.

The robust, single-step diagnostic platform that was developed demonstrated automated and sequential delivery of biomarkers and enzymatic signal enhancement reagents in a consistent manner. In the future, this platform technology can be extended to other enzymatic signal enhancement systems to transform diagnostic assays for chlamydia and other diseases.

3.2   Materials and Methods

3.2.1   Preparation of EOPO-salt ATPS

To prepare the ATPS solution, mixtures of poly(ethylene glycol-*ran*-propylene glycol) (EOPO; MW ~12,000; Sigma-Aldrich, St. Louis, MO) and sodium sulfate salt (Sigma-Aldrich, St. Louis, MO) were dissolved in Dulbecco's phosphate-buffered saline (PBS; Invitrogen, Grand Island, NY). A final overall concentration of 15% EOPO and 4% sodium sulfate salt was used for the diagnostic test.

3.2.2   Preparation of Anti-CT antibody- and Enzyme- decorated Gold Nanoprobes (anti-CT-ALP-GNPs)

To form nanoprobes decorated with ALP, 1 mL of 40 nm gold nanoparticles (nanoComposix, San Diego, CA) was adjusted to a pH of 8 using 0.1 M sodium borate. Then, 1 μg of ALP was added to the gold suspension and incubated for 5 minutes at room temperature. Subsequently, 8 μg of antibodies specific to CT (MyBioSource, San Diego, CA) was added and incubated for 25 minutes at room temperature. Subsequently, 100 uL of 10% BSA was added and incubated for 10 min. The gold nanoprobes decorated with ALP were purified four times by centrifuging at 6000 rpm for 6 minutes each.

3.2.3 Partitioning of Enzymes and Substrates in ATPS

In order to visually verify the partitioning of enzymes conjugated to gold nanoprobes in an ATPS, 20 µL of anti-CT-ALP-GNPs were added to a 1 mL EOPO/sodium sulfate ATPS. Similarly, the partitioning of the substrate NBT was visually verified by adding 6.6 µL of NBT/BCIP to a 1 mL ATPS. The solutions were vortexed thoroughly and allowed to phase separation at room temperature for 30 minutes. Pictures were taken at 20 minutes using a Canon EOS 1000D camera (Canon U.S.A., Inc., Lake Success, NY) in a controlled lighting environment.

3.2.4 Preparation of Conjugate Pads with Dehydrated anti-CT-ALP-GNPs

A suspension of anti-ALP-GNPs containing 1% BSA was spotted onto 3 mm x 10 mm fiberglass paper (GE Healthcare Life Sciences, Marlborough, MA). The paper was then vacuum-dried with a benchtop lyophilizer (Labconco, Kansas City, MO) for 30 minutes until completely dry.

3.2.5 Fabrication of acrylic housing

To fabricate the three-piece acrylic housing, clear sheets of acrylic (McMaster-Carr, Santa Fe Springs, CA) were cut with a CO_2 laser cutter system (Universal Laser Systems U.S.A., Inc., Scottsdale, AZ). The top and bottom pieces consisted of full pieces of acrylic, and the center piece was designed with a cutout such that the casing would conform to the test strip dimensions. This was mounted on the bottom rectangular piece in order to form a trough to hold the test strip. A 4 mm x 10 mm foam piece (McMaster-Carr, Santa Fe Springs, CA) was added to the top acrylic piece such that it would be placed on the interface between the conjugate pad and the membrane. The height of the foam piece was modulated with laser-cut 4 mm x 10 mm sheets of adhesive PET

film (Adhesives Research, Glen Rock, PA). In addition, the casing was fabricated in such a way that the three pieces held the stacks of the LFA wick together. The pieces of the acrylic housing were held together by Scotch double sided tape (3M, St. Paul, MN, USA).

3.2.6 Detection of CT with ATPS-mediated Delivery and Enzymatic Signal Enhancement

LFA test strips utilizing the sandwich assay format were assembled similarly to previous studies [22], [75]. Antibodies specific to CT (MyBioSource, San Diego, CA) were immobilized on backed nitrocellulose membrane by striping a solution of the antibodies containing 25% sucrose (Sigma-Aldrich, St. Louis, MO). This constituted the test line of the test strip. Protein A (Sigma-Aldrich, St. Louis, MO) was similarly immobilized to constitute the control line of the test. The nitrocellulose membrane was cut into strips 3 mm in width.

The design of the LFA test strip was modified to include the addition of a vertical paper well. This larger wick was composed of four stacks of 7 mm x 10 mm fiberglass paper (GE Healthcare Life Sciences, Marlborough, MA). The fiberglass paper was treated by adding a solution of 0.1% BSA and 0.001% Tween 20 (Sigma-Aldrich, St. Louis, MO) and vacuum-drying with a benchtop lyophilizer (Labconco, Kansas City, MO) for 30 min. A cellulose absorbent pad (GE Healthcare Life Sciences, Marlborough, MA) was placed downstream of the nitrocellulose membrane. Once assembled, the test strip was enclosed in the custom acrylic housing.

For detection of CT, 500 µL of a well-mixed ATPS containing CT, NBT, and BCIP were added to a well in a 24-well plate (Corning Inc., Corning, NY). The test strip enclosed in the custom acrylic housing was then placed in the mixed solution. The fluid was allowed to wick up vertically through the wick. Images of the detection region were captured at various time points

using a Canon EOS 1000D camera (Canon U.S.A., Inc., Lake Success, NY) in a controlled lighting environment.

3.3   Results and Discussion

3.3.1   Partitioning of Enzyme and Substrate into Different Phases

Effective separation of enzyme and substrates via partitioning in ATPS was first verified using the methods described previously. Anti-CT-ALP-GNPs were large enough to have excluded-volume interactions with the large EOPO molecules in the top, EOPO-rich phase, and partitioned preferentially into the bottom, salt-rich phase. This is shown on the left side of **Fig. 3.1** with the cherry red-colored anti-CT-ALP-GNPs predominantly in the bottom phase. The hydrophobic NBT, on the other hand, partitioned preferentially into the top, EOPO-rich phase due to the relative hydrophobicity of that phase. This is shown on the right side of **Fig. 3.1** with the yellow NBT substrate predominantly in the top phase. By choosing an ATPS in which the enzyme conjugated to gold nanoprobes partitioned into a phase opposite from its substrate, we prevented premature enzymatic signal enhancement.
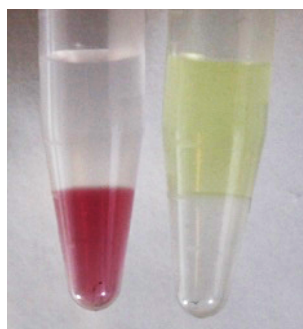
Fig 3.1 Partitioning of enzyme and substrate in ATPS. *Anti-CT-ALP-GNPs partitioned preferentially into the bottom, salt-rich phase (left), and NBT partitioned preferentially into the top, polymer-rich phase (right), effectively preventing premature enzymatic signal enhancement.*

3.3.2   Improved Conjugate Release and Background with Development of Acrylic Housing

An acrylic housing was developed for our diagnostic platform that fine-tuned fluid flow

through the test strip and allowed for consistent release of anti-CT-ALP-GNPs from the conjugate pad to allow consistent delivery of nanoprobes to the detection region. This acrylic housing was designed in such a way that the test strip would snugly fit in the center of the bottom piece (**Fig 3.2a**). The addition of the top piece of the housing would then function to fully enclose the test strip from the elements and prevent evaporation effects from changing flow patterns and disrupting the controlled delivery of reagents in the paper-based immunoassay. In addition, once the housing was closed, it applied light pressure on the many stacks of fiberglass paper that constituted the wick, and held together the paper strips. Moreover, the top of the housing was designed with an extra extruded foam portion placed in such a way that closing the top piece over the bottom piece would exert slight pressure on the test strip at the interface between the conjugate pad and membrane (**Fig 3.2a**). The height of the foam was adjusted such that enough pressure was exerted without overexerting pressure and crushing the integrity of the paper. The final design for the integrated platform technology is shown in **Fig 3.2b**.
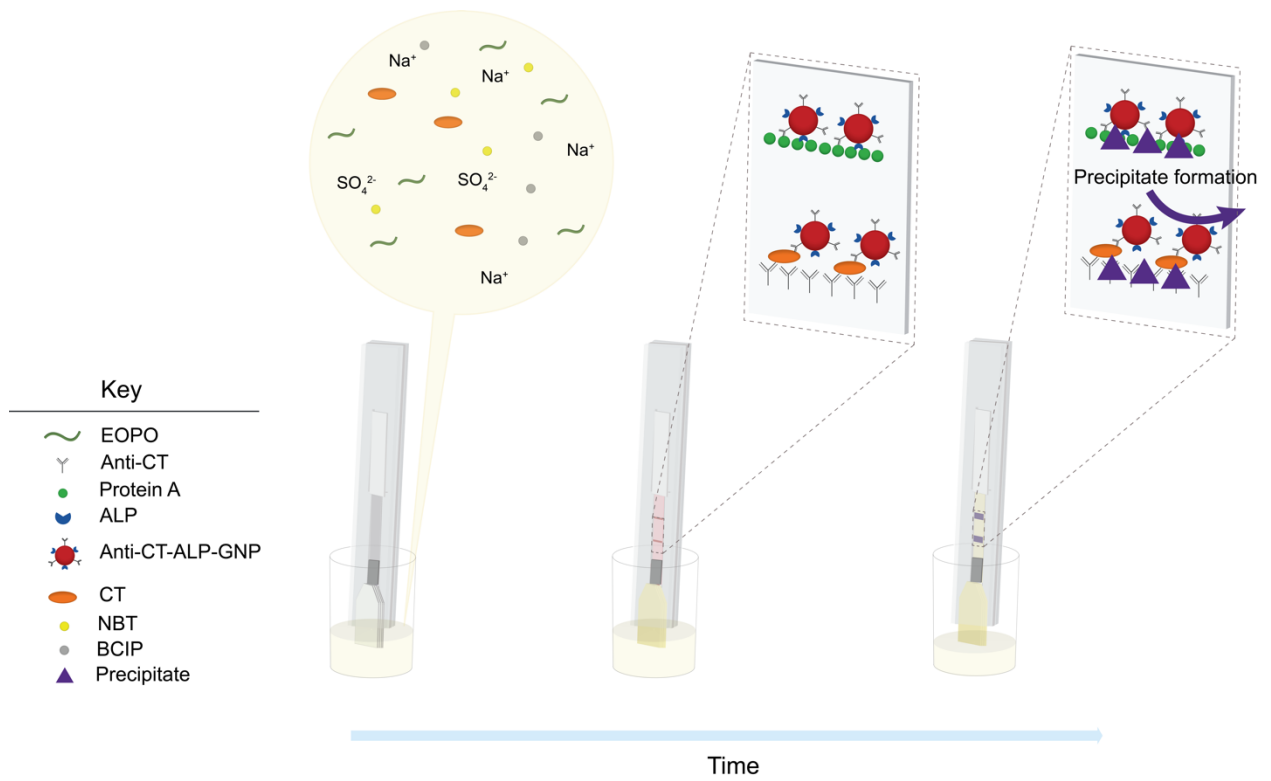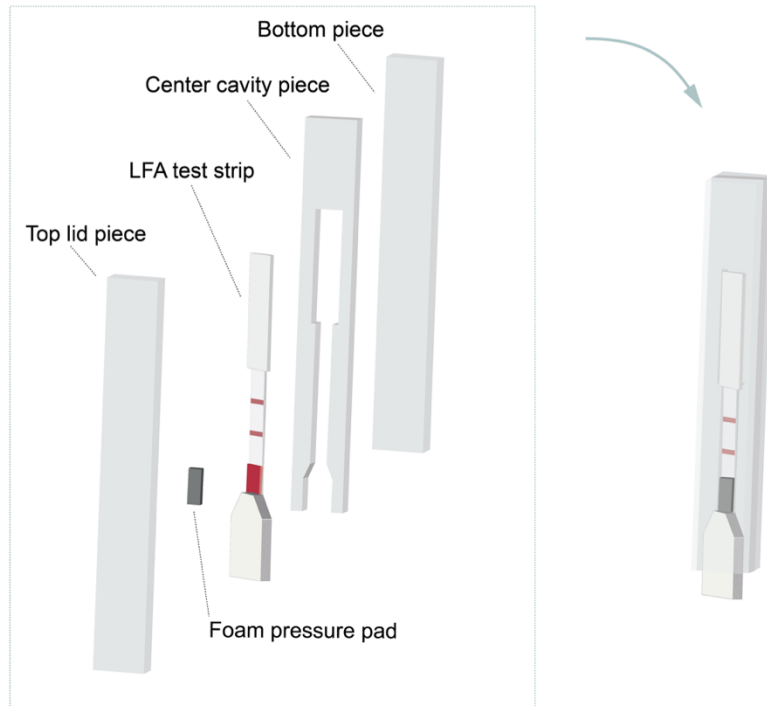
(a)

**Fig 3.2** Integration of ATPS and casing with the LFA.

Controlled pressure on the conjugate pad and wick was shown to benefit the release of dehydrated anti-CT-ALP-GNPs from the conjugate pad. After tests were run, images were taken of the resulting interface between the conjugate pad and the membrane. When no pressure was placed on the conjugate pad, the release of the conjugates during rehydration was incomplete, as indicated by dark conjugates stuck at the interface (**Fig 3.3a**). We hypothesize that a lack of pressure and thus lack of proper contact between the conjugate pad and membrane resulted in this type of pattern formation. The poor contact resulted in fluid flow that was too slow, which in turn allowed more time for the anti-CT-ALP-GNPs to collect and bind nonspecifically to the edges of the paper pad interface between the conjugate pad and membrane. This is corroborated by the literature, as housings designed with inconsistent pressure points have been shown to result in variations in fluid flow, and thus a consistent design is necessary [76], [77]. Conversely, when a proper amount of pressure is placed on the pad to ensure proper contact between the conjugate pad and the nitrocellulose membrane, the result was clean, even release of the conjugates (**Fig 3.3b**). By modulating the height of the foam piece on the top part of the housing, we optimized the pressure exerted on the interface between the conjugate pad and membrane and consistently controlled the fluid flow through that interface.
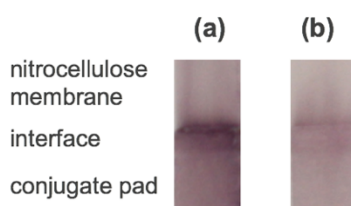
Fig 3.3 Control of conjugate release from the conjugate pad. *The release of anti-CT-ALP-GNPs was modified by application of conjugate pad pressure. No pressure (a) results in incomplete conjugate release, while controlled even pressure (b) results in sustained and complete release.*

Furthermore, controlling the environment with the acrylic housing was shown to be beneficial toward preventing background on the nitrocellulose membrane detection zone. As shown in Fig **3.4a**, failure to enclose the test strip results in a dark, streaky background. We hypothesized that leaving the test strip open to the air results in greater evaporation from the test

strip, which prevents efficient delivery of the anti-CT-ALP-GNPs across the nitrocellulose detection zone. This was corroborated by previous studies in the literature, in which evaporation had been shown to slow fluid flow [18], [78]. Similar patterns of particle deposition from drying effects have been reported in the literature as well [79]–[81]. As the test fluid evaporated during the test, anti-CT-ALP-GNPs were deposited nonspecifically on the nitrocellulose membrane rather than fully flowing downstream to the absorbent pad. The combined effect was an increase in nonspecific signals on the detection zone and a highly noisy background. On the contrary, placing the test strip in a controlled environment casing protected the test from significant evaporation and resulted in a clean, even background (**Fig 3.4b**). The fabrication of a consistent acrylic housing for this system thus improved delivery of biomolecules in the LFA.
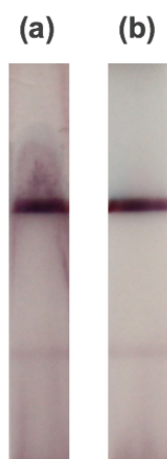
Fig 3.4 Effect of controlled environment on LFA background. *Running an LFA test without the casing resulted in a streaky background (a), while the use of a custom casing to provide a controlled environment resulted in a clean background (b).*

3.3.3 Automated sequential delivery of signal enhancement reagents with ATPS

Using our optimized system, we achieved automated, sequential delivery of enzymatic signal enhancement components in the ATPS. Shown in **Fig 3.5** is the detection zone of an LFA test run at a concentration of 1 ng/μL of CT with our finalized design over three different time points. The start of the test was captured and shown in the left panel of **Fig 3.5.** At this point, the

test was dipped into the sample ATPS solution, and phase separation began through the paper wick. No fluid was yet delivered to the detection zone at this point, so no lines were present.

During the first delivery phase, the leading salt-rich phase of the ATPS was delivered to the detection zone. The end of this first step was captured and shown in the center panel of **Fig 3.5**. At this point, there was conjugate binding to the test and control lines, and the color was the cherry red of the anti-CT-ALP-GNPs. This indicated that anti-CT-ALP-GNPs were successfully delivered to the detection zone. In addition, due to the color of the line, the image indicated that no enzymatic signal enhancement had begun at this point, and thus the partitioning of the enzyme and its substrates to opposite phases of the ATPS was successful in the integrated paper format. During the second delivery phase, the polymer-rich phase of the ATPS was delivered to the detection zone. The end of the second ATPS delivery phase was captured at 30 min and is shown in the right panel of **Fig 3.5**. During this delivery phase, the NBT/BCIP in the polymer-rich phase were delivered to the detection zone, and the ALP immobilized on the test and control lines cleaved the substrates to form a dark purple precipitate. This was deposited at the locations of the test and control lines, as shown in the darkened purple lines in the image. Compared to the test line after the first delivery step, the resulting test line after the second delivery step is visually much darker, indicating successful enzymatic signal enhancement.

These results indicated that the integrated platform technology for automated enzymatic signal enhancement was successfully achieved. The ATPS successfully partitioned the enzyme and substrates into opposite phases and delivered them sequentially to the detection zone, thus enhancing the signal intensities at the test and control lines.
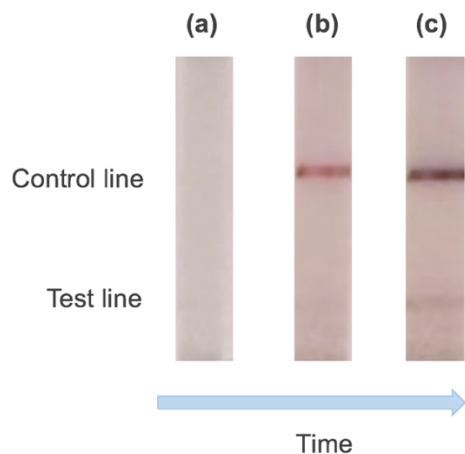
Fig 3.5 Automated enzymatic signal enhancement over time. *Signal enhancement reagents were delivered to the detection zone in an automated multistep fashion. The detection zone is shown before biomolecule delivery (left), after delivery of the anti-CT-ALP-GNPs and CT (center), and after delivery of enzymatic substrates (right). Darkening of the test lines indicates successful implementation of enzymatic signal enhancement.*

3.4   Conclusion

Controlled delivery of biomolecules in paper-based immunoassays is essential for achieving multistep LFA and improving sensitivity. In this work, we used an ATPS to automate the delivery of enzymatic signal enhancement components to the detection zone of an LFA. The enzyme was separated from its substrates through their partitioning behaviors in the ATPS to prevent premature enzymatic signal enhancement. Each of the components were then delivered sequentially via the ATPS phase separation phenomenon on paper. Furthermore, an acrylic housing was fabricated to fully enclose the test strip and minimize evaporation effects, and the housing was further modified so that adequate pressure would be generated to make sufficient contact between the conjugate pad and membrane. The contact generated a sufficient fluid flow path through the paper test strip and allowed for consistent conjugate delivery. With this design, our optimized integrated platform technology demonstrated precise control of a multistep enzymatic signal enhancement assay in a paper-based diagnostic system. In the future, this technology can be extended to other multistep assays to improve the sensitivity of LFA even further.

63

References

[1]   R. L. Siegel, K. D. Miller, and A. Jemal, "Cancer statistics, 2017," *CA. Cancer J. Clin.*, vol. 67, no. 1, pp. 7–30, 2017.

[2]   T. R. Daniels, T. Delgado, G. Helguera, and M. L. Penichet, "The transferrin receptor part II: Targeted delivery of therapeutic agents into cancer cells," *Clin. Immunol.*, vol. 121, no. 2, pp. 159–176, 2006.

[3]   R. V. J. Chari, "Targeted cancer therapy: Conferring specificity to cytotoxic drugs," *Acc. Chem. Res.*, vol. 41, no. 1, pp. 98–107, 2008.

[4]   A. Thomas, B. A. Teicher, and R. Hassan, "Antibody-drug conjugates for cancer therapy," *Lancet Oncol.*, vol. 17, no. 6, pp. e254–e262, 2016.

[5]   L. Brannon-Peppas and J. O. Blanchette, "Nanoparticle and targeted systems for cancer therapy," *Adv. Drug Deliv. Rev.*, vol. 64, pp. 206–212, 2012.

[6]   S. C. Alley, N. M. Okeley, and P. D. Senter, "Antibody-drug conjugates: Targeted drug delivery for cancer," *Curr. Opin. Chem. Biol.*, vol. 14, no. 4, pp. 529–537, 2010.

[7]   A. Parslow, S. Parakh, F.-T. Lee, H. Gan, and A. Scott, "Antibody–Drug Conjugates for Cancer Therapy," *Biomedicines*, vol. 4, no. 3, p. 14, 2016.

[8]   D. P. O'Neal, L. R. Hirsch, N. J. Halas, J. D. Payne, and J. L. West, "Photo-thermal tumor ablation in mice using near infrared-absorbing nanoparticles," *Cancer Lett.*, vol. 209, no. 2, pp. 171–176, 2004.

[9]   Y. Nakamura, A. Mochida, P. L. Choyke, and H. Kobayashi, "Nanodrug Delivery: Is the Enhanced Permeability and Retention Effect Sufficient for Curing Cancer?," *Bioconjug. Chem.*, vol. 27, no. 10, pp. 2225–2238, 2016.

[10]   J. Cassidy and A. G. Schätzlein, "Tumour-targeted drug and gene delivery: principles and concepts.," *Expert Rev. Mol. Med.*, vol. 6, no. 19, pp. 1–17, 2004.

[11]   L. van Dommelen, F. H. van Tiel, S. Ouburg, E. E. H. G. Brouwers, P. H. W. Terporten, P. H. M. Savelkoul, S. a Morré, C. a Bruggeman, and C. J. P. a Hoebe, "Alarmingly poor performance in Chlamydia trachomatis point-of-care testing.," *Sex. Transm. Infect.*, vol. 86, no. 5, pp. 355–359, 2010.

[12]   J. Walker, S. N. Tabrizi, C. K. Fairley, M. Y. Chen, C. S. Bradshaw, J. Twin, N. Taylor, B. Donovan, J. M. Kaldor, K. McNamee, E. Urban, S. Walker, M. Currie, H. Birden, F. Bowden, J. Gunn, M. Pirotta, L. Gurrin, V. Harindra, S. M. Garland, and J. S. Hocking, "Chlamydia trachomatis incidence and re-infection among young women - behavioural and microbiological characteristics," *PLoS One*, vol. 7, no. 5, pp. 1–9, 2012.

[13]   D. C. Young, S. Craft, M. Day, B. Davis, E. Hartwell, and S. Tong, "Comparison of Abbott LCx Chlamydia trachomatis Assay With Gen-Probe PACE2 and Culture," vol. 115, no. July 1999, pp. 112–115, 2000.

[14] S. F. Cheung, S. K. L. Cheng, and D. T. Kamei, "Paper-Based Systems for Point-of-Care Biosensing," *J. Lab. Autom.*, vol. 20, no. 4, pp. 316–333, 2015.

[15] G. E. Fridley, H. Le, and P. Yager, "Highly sensitive immunoassay based on controlled rehydration of patterned reagents in a 2-dimensional paper network," *Anal. Chem.*, vol. 86, no. 13, pp. 6447–6453, 2014.

[16] W. Wang, *Lyophilization and development of solid protein pharmaceuticals*, vol. 203. 2000.

[17] D. Y. Stevens, D. Y. Stevens, C. R. Petri, C. R. Petri, P. Yager, and P. Yager, "On-card dry reagent storage for disposable microfluidic immunoassays," *Lab Chip*, pp. 188–190, 2008.

[18] H. Noh and S. T. Phillips, "Fluidic timers for time-dependent, point-of-care assays on paper," *Anal. Chem.*, vol. 82, no. 19, pp. 8071–8078, 2010.

[19] S. Ramachandran, E. Fu, B. Lutz, and P. Yager, "Long-term dry storage of an enzyme-based reagent system for ELISA in point-of-care devices," *Analyst*, vol. 139, no. 6, pp. 1456–62, 2014.

[20] S. Ohtake and J. Y. Wang, "Trehalose: Current Use and Future Applications," *J. Pharm. Sci.*, vol. 99, no. 10, pp. 4215–4227, 2010.

[21] C. A. Holstein, A. Chevalier, S. Bennett, C. E. Anderson, K. Keniston, C. Olsen, B. Li, B. Bales, D. R. Moore, E. Fu, D. Baker, and P. Yager, "Immobilizing affinity proteins to nitrocellulose: a toolbox for paper-based assay developers," *Anal. Bioanal. Chem.*, pp. 1335–1346, 2015.

[22] D. Y. Pereira, R. Y. T. Chiu, S. C. L. Zhang, B. M. Wu, and D. T. Kamei, "Single-step, paper-based concentration and detection of a malaria biomarker," *Anal. Chim. Acta*, vol. 882, pp. 83–89, 2015.

[23] V. Gubala, L. F. Harris, A. J. Ricco, M. X. Tan, and D. E. Williams, "Point of care diagnostics: Status and future," *Anal. Chem.*, vol. 84, no. 2, pp. 487–515, 2012.

[24] E. Fu, T. Liang, J. Houghtaling, S. Ramachandran, S. A. Ramsey, B. Lutz, and P. Yager, "Enhanced Sensitivity of Lateral Flow Tests Using a Two-Dimensional Paper Network Format," *Anal. Chem.*, no. 83, pp. 7941–7946, 2011.

[25] C. Parolo, A. de la Escosura-Muñiz, and A. Merkoçi, "Enhanced lateral flow immunoassay using gold nanoparticles loaded with enzymes," *Biosens. Bioelectron.*, vol. 40, pp. 412–416, 2012.

[26] R. Gerbers, W. Foellscher, H. Chen, C. Anagnostopoulos, and M. Faghri, "A New Paper-Based Platform Technology for Point-of-Care Diagnostics," *Lab Chip*, vol. 14, pp. 4042–4049, 2014.

[27] I.-H. Cho, A. Bhunia, and J. Irudayaraj, "Rapid pathogen detection by lateral-flow immunochromatographic assay with gold nanoparticle-assisted enzyme signal

amplification," *Int. J. Food Microbiol.*, vol. 206, pp. 60–66, 2015.

[28] P. Y. Elain Fu, Tinny Liang, Paolo Spicar-Mihalic, Jared Houghtaling, Sujatha Ramachandran, "A two-dimensional paper network format that enables simple multi-step assays for use in low-resource settings in the context of malaria antigen detection," *Anal Chem*, vol. 84, no. 10, pp. 4574–4579, 2012.

[29] K. N. Han, J.-S. Choi, J. Kwon, V. Gubala, L. F. Harris, A. J. Ricco, M. X. Tan, D. E. Williams, K. N. Han, C. A. Li, G. H. Seong, R. Safavieh, D. Juncker, A. M. Foudeh, Fatanat, T. Didar, T. Veres, M. Tabrizian, G. G. Lewis, J. S. Robbins, S. T. Phillips, A. W. Martinez, S. T. Phillips, G. M. Whitesides, E. Carrilho, J. Hu, X. Wei, B. Ngom, Y. Guo, X. Wang, D. Bi, X. Ge, C. Parolo, A. de la Escosura-Muñiz, A. Merkoçi, B. A. Rohrman, V. Leautaud, E. Molyneux, R. R. Richards-Kortum, L. Ge, A. W. Martinez, S. T. Phillips, G. M. Whitesides, A. C. Glavan, H. Liu, R. M. Crooks, E. Fu, H. Liu, X. Li, R. M. Crooks, Y. K. Oh, H. A. Joung, S. Kim, M. G. Kim, J. C. Cunningham, N. J. Brenes, R. M. Crooks, E. Robilotti, S. Deresinski, B. A. Pinsky, J. Vinjé, K. F. Lei, Y. K. C. Butt, Y. Li, C. Zhang, D. Xing, V. Costantini, K. Pombubpa, L. Kittigul, H. S. Kim, and A. E. Hagström, "Three-dimensional paper-based slip device for one-step point-of-care testing," *Nat. Sci. Reports*, vol. 6, no. February, pp. 1–7, 2016.

[30] E. Fu, B. Lutz, P. Kauffman, and P. Yager, "Controlled reagent transport in disposable 2D paper networks," *Lab Chip*, vol. 10, no. 7, p. 918, 2010.

[31] B. J. Toley, B. McKenzie, T. Liang, J. R. Buser, P. Yager, and E. Fu, "Tunable-Delay Shunts for Paper Microfluidic Devices," *Anal. Chem.*, vol. 85, no. 23, pp. 11545–52, 2013.

[32] H. Chen, J. Cogswell, C. Anagnostopoulos, and M. Faghri, "A fluidic diode, valves, and a sequential-loading circuit fabricated on layered paper," *Lab Chip*, vol. 12, no. 16, p. 2909, 2012.

[33] A. Jelińska, A. Zagożdżon, M. Gorecki, A. Wisniewska, J. Frelek, and R. Holyst, "Denaturation of proteins by surfactants studied by the Taylor dispersion analysis," *PLoS One*, pp. 1–11, 2017.

[34] B. Lutz, T. Liang, E. Fu, S. Ramachandran, P. Kauffman, and P. Yager, "Dissolvable fluidic time delays for programming multi-step assays in instrument-free paper diagnostics." *Lab Chip*, vol. 13, no. 14, pp. 2840–7, 2013.

[35] S. Jahanshahi-Anbuhi, A. Henry, V. Leung, C. Sicard, K. Pennings, R. Pelton, J. D. Brennan, and C. D. M. Filipe, "Paper-based microfluidics with an erodible polymeric bridge giving controlled release and timed flow shutoff," *Lab Chip*, vol. 14, no. 1, pp. 229–236, 2014.

[36] R. L. Siegel, K. D. Miller, and A. Jemal, "Cancer statistics," vol. 66, no. 1, pp. 7–30, 2016.

[37] P. Cazzola, Mario; Bergamaschi Gaetano; Dezza Laura; Arosio, "Manipulations of cellular iron metabolisms for modulating normal and malignant cell proliferation:

Achievements and prospects," *J. Am. Soc. Hematol.*, vol. 75, no. 10, pp. 1903–1919, 1990.

[38] P. Ponka and C. N. Lok, "The transferrin receptor: role in health and disease," *Int. J. Biochem. Cell Biol.*, vol. 31, no. 10, pp. 1111–1137, 1999.

[39] V. G. Johnson, D. Wilson, L. Greenfield, and R. J. Youle, "The role of the diphtheria toxin receptor in cytosol translocation," *J. Biol. Chem.*, vol. 263, no. 3, pp. 1295–1300, 1988.

[40] R. D. Klausner, G. Ashwell, J. O. S. V. A. N. Renswoude, J. O. E. B. Harford, and K. R. Bridges, "Binding of apotransferrin to K562 cells : Explanation of the transferrin cycle," *Proc. Natl. Acad. Sci.*, vol. 80, no. April, pp. 2263–2266, 1983.

[41] A. Ciechanover, A. L. Schwartz, and H. F. Lodish, "Sorting and Recycling of Cell Surface Receptors and Endocytosed Ligands : The Asialoglycoprotein and Transferrin Receptors," vol. 130, pp. 107–130, 1983.

[42] Z. M. Qian, "Targeted Drug Delivery via the Transferrin Receptor-Mediated Endocytosis Pathway," *Pharmacol. Rev.*, vol. 54, no. 4, pp. 561–587, 2002.

[43] P. T. Yazdi and R. M. Murphy, "Quantitative analysis of protein synthesis inhibition by transferrin- toxin conjugates," *Cancer Res.*, vol. 54, no. 24, pp. 6387–6394, 1994.

[44] B. J. Lao and D. T. Kamei, "Investigation of cellular movement in the prostate epithelium using an agent-based model," *J. Theor. Biol.*, vol. 250, no. 4, pp. 642–654, 2008.

[45] B. J. Lao, W. L. P. Tsai, F. Mashayekhi, E. A. Pham, A. B. Mason, and D. T. Kamei, "Inhibition of transferrin iron release increases in vitro drug carrier efficacy," *J. Control. Release*, vol. 117, no. 3, pp. 403–412, 2007.

[46] D. J. Yoon, B. H. Kwan, F. C. Chao, T. P. Nicolaides, J. J. Phillips, G. Y. Lam, A. B. Mason, W. A. Weiss, and D. T. Kamei, "Intratumoral therapy of glioblastoma multiforme using genetically engineered transferrin for drug delivery," *Cancer Res.*, vol. 70, no. 11, pp. 4520–4527, 2010.

[47] D. J. Yoon, D. S. H. Chu, C. W. Ng, E. A. Pham, A. B. Mason, D. M. Hudson, V. C. Smith, R. T. A. MacGillivray, and D. T. Kamei, "Genetically engineering transferrin to improve its in vitro ability to deliver cytotoxins," *J. Control. Release*, vol. 133, no. 3, pp. 178–184, 2009.

[48] R. J. Collier, "Diphtheria toxin: mode of action and structure.," *Bacteriol. Rev.*, vol. 39, no. 1, pp. 54–85, 1975.

[49] V. G. Johnson, C. Wrobel, D. Wilson, J. Zovickian, L. Greenfield, E. H. Oldfield, and R. Youle, "Improved tumor-specific immunotoxins in the treatment of CNS and leptomeningeal neoplasia," *J Neurosurg*, vol. 70, no. 2, pp. 240–248, 1989.

[50] K. Goishi, S. Higashiyama, M. Klagsbrun, N. Nakano, T. Umata, M. Ishikawa, E. Mekada, and N. Taniguchi, "Phorbol ester induces the rapid processing of cell surface heparin-binding EGF-like growth factor: conversion from juxtacrine to paracrine growth

factor activity.," *Mol. Biol. Cell*, vol. 6, no. 8, pp. 967–80, 1995.

[51]   B. J. Rönnberg and J. L. Middlebrook, "Cellular regulation of diphtheria toxin cell surface receptors," *Toxicon*, vol. 27, no. 12, pp. 1377–1388, 1989.

[52]   M. Yamaizumi, T. Uchida, K. Takamatsu, and Y. Okada, "Intracellular stability of diphtheria toxin fragment A in the presence and absence of anti-fragment A antibody.," *Proc. Natl. Acad. Sci. U. S. A.*, vol. 79, no. 2, pp. 461–5, 1982.

[53]   B. Dorland and L. Middlebrook, "Receptor-mediated internalization and degradation of diphtheria toxin by monkey kidney cells," *J. Biol. Chem.*, vol. 254, no. 22, pp. 11337–11342, 1979.

[54]   J. L. Middlebrook, R. B. Dorland, and S. H. Leppla, "Association of diphtheria toxin with Vero cells," *J. Biol. Chem.*, vol. 253, no. 20, pp. 7325–7330, 1978.

[55]   E. Papini, R. Rappuoli, M. Murgia, and C. Montecucco, "Cell penetration of diphtheria toxin," *J. Biol. Chem.*, vol. 268, no. 3, pp. 1567–1574, 1993.

[56]   R. Iwamoto, S. Higashiyama, T. Mitamura, N. Taniguchi, M. Klagsbrun, and E. Mekada, "Heparin-binding EGF-like growth factor, which acts as the diphtheria toxin receptor, forms a complex with membrane protein DRAP27/CD9, which up-regulates functional receptors and diphtheria toxin sensitivity.," *EMBO J.*, vol. 13, no. 10, pp. 2322–30, 1994.

[57]   T. Mitamura, S. Higashiyama, N. Taniguchi, M. Klagsbrun, and E. Mekada, "Diphtheria toxin binds to the epidermal growth factor (EGF)-like domain of human heparin-binding EGF-like growth factor/diphtheria toxin receptor and inhibits specifically its mitogenic activity," *Journal of Biological Chemistry*, vol. 270, no. 3. pp. 1015–1019, 1995.

[58]   K. M. Gallegos, D. G. Conrady, S. S. Karve, T. S. Gunasekera, A. B. Herr, and A. A. Weiss, "Shiga toxin binding to glycolipids and glycans," *PLoS One*, vol. 7, no. 2, 2012.

[59]   a R. French and D. a Lauffenburger, "Controlling receptor/ligand trafficking: effects of cellular and molecular properties on endosomal sorting.," *Ann. Biomed. Eng.*, vol. 25, no. 4, pp. 690–707, 1997.

[60]   A. Ciechanover, A. L. Schwartzgll, A. Dautry-varsat, and H. F. Lodish, "Transferrin receptor in a human hepatoma cell line," *J. Biol. Chem.*, vol. 258, no. 16, pp. 9681–9689, 1983.

[61]   P. J. Halbrooks, Q.-Y. He, S. K. Briggs, S. J. Everse, V. C. Smith, R. T. A. MacGillivray, and A. B. Mason, "Investigation of the Mechanism of Iron Release from the C-Lobe of Human Serum Transferrin: Mutational Analysis of the Role of a pH Sensitive Triad [†]," *Biochemistry*, vol. 42, no. 13, pp. 3701–3707, 2003.

[62]   A. R. French and D. A. Lauffenburger, "Intracellular receptor/ligand sorting based on endosomal retention components," *Biotechnol. Bioeng.*, vol. 34, no. 7, pp. 281–297, 1996.

[63]   F. Kilár and I. Simon, "The effect of iron binding on the conformation of transferrin. A small angle x-ray scattering study.," *Biophys. J.*, vol. 48, no. 5, pp. 799–802, 1985.

[64] S. Choe, M. J. Bennett, G. Fujii, P. M. Curmi, K. a Kantardjieff, R. J. Collier, and D. Eisenberg, "The crystal structure of diphtheria toxin," *Nature*, vol. 357, no. 6375, pp. 216–222, 1992.

[65] M. Marsh, G. Griffiths, G. E. Dean, I. Mellman, and a Helenius, "Three-dimensional structure of endosomes in BHK-21 cells.," *Proc. Natl. Acad. Sci. U. S. A.*, vol. 83, no. 9, pp. 2899–903, 1986.

[66] A. Chenal, L. Prongidi-Fix, A. Perier, C. Aisenbrey, G. Vernier, S. Lambotte, G. Fragneto, B. Bechinger, D. Gillet, V. Forge, and M. Ferrand, "Deciphering membrane insertion of the diphtheria toxin T domain by specular neutron reflectometry and solid-state NMR spectroscopy," *J. Mol. Biol.*, vol. 391, no. 5, pp. 872–883, 2009.

[67] A. Dautry-Varsat, A. Ciechanover, and H. F. Lodish, "pH and the recycling of transferrin during receptor-mediated endocytosis," *Proc. Natl. Acad. Sci.*, vol. 80, no. April, pp. 2258–2262, 1983.

[68] C. Watts, "Rapid endocytosis of the transferrin receptor in the absence of bound transferrin," *J. Cell Biol.*, vol. 100, no. 2, pp. 633–637, 1985.

[69] W. Laird and N. Groman, "Isolation and characterization of tox mutants of corynebacteriophage beta," *J Virol*, vol. 19, no. 1, pp. 220–227, 1976.

[70] A. B. Mason, Q. Y. He, P. J. Halbrooks, S. J. Everse, D. R. Gumerov, I. A. Kaltashov, V. C. Smith, J. Hewitt, and R. T. A. MacGillivray, "Differential effect of a His tag at the N- and C-termini: Functional studies with recombinant human serum transferrin," *Biochemistry*, vol. 41, no. 30, pp. 9448–9454, 2002.

[71]   a B. Mason, Q. Y. He, T. E. Adams, D. R. Gumerov, I. a Kaltashov, V. Nguyen, and R. T. MacGillivray, "Expression, purification, and characterization of recombinant nonglycosylated human serum transferrin containing a C-terminal hexahistidine tag.," *Protein Expr. Purif.*, vol. 23, no. 1, pp. 142–150, 2001.

[72] R. D. Klausner, J. Vanrenswoude, G. Ashwell, C. Kempf, a N. Schechter, a Dean, and K. R. Bridges, "Receptor-Mediated Endocytosis of Transferrin in K562-Cells," *J. Biol. Chem.*, vol. 258, no. 8, pp. 4715–4724, 1983.

[73] F. Mashayekhi, A. M. Le, P. M. Nafisi, B. M. Wu, and D. T. Kamei, "Enhancing the lateral-flow immunoassay for detection of proteins using an aqueous two-phase micellar system," *Anal. Bioanal. Chem.*, vol. 404, no. 6–7, pp. 2057–2066, 2012.

[74] E. Jue, C. D. Yamanishi, R. Y. T. Chiu, B. M. Wu, and D. T. Kamei, "Using an aqueous two-phase polymer-salt system to rapidly concentrate viruses for improving the detection limit of the lateral-flow immunoassay," *Biotechnol. Bioeng.*, vol. 111, no. 12, pp. 2499–2507, 2014.

[75] R. Y. T. Chiu, E. Jue, A. T. Yip, A. R. Berg, S. J. Wang, A. R. Kivnick, P. T. Nguyen, D. T. Kamei, P. Yager, G. J. Domingo, J. Gerdes, C. A. Petti, C. R. Polage, T. C. Quinn, A. R. Ronald, M. A. Sande, P. Yager, T. Edwards, E. Fu, K. Helton, K. Nelson, M. R. Tam,

B. H. Weigl, E. Fu, T. Liang, J. Houghtaling, S. Ramachandran, S. A. Ramsey, B. Lutz, P. Yager, E. Fu, T. Liang, P. Spicar-Mihalic, J. Houghtaling, S. Ramachandran, P. Yager, C. M. Cheng, A. W. Martinez, J. Gong, C. R. Mace, S. T. Phillips, E. Carrilho, K. A. Mirica, G. M. Whitesides, J. L. Osborn, B. Lutz, E. Fu, P. Kauffman, D. Y. Stevens, P. Yager, H. Noh, S. T. Phillips, B. R. Lutz, P. Trinh, C. Ball, E. Fu, P. Yager, H. Noh, S. T. Phillips, B. Lutz, T. Liang, E. Fu, S. Ramachandran, P. Kauffman, P. Yager, X. Li, P. Zwanenburg, X. Liu, F. Mashayekhi, R. Y. Chiu, A. M. Le, F. C. Chao, B. M. Wu, D. T. Kamei, F. Mashayekhi, A. M. Le, P. M. Nafisi, B. M. Wu, D. T. Kamei, H. Jang, S. R. Ryoo, K. Kostarelos, S. W. Han, D. H. Min, P. N. Njoki, I. I. S. Lim, D. Mott, H. Y. Park, B. Khan, S. Mishra, R. Sujakumar, J. Luo, C. J. Zhong, M. C. Daniel, D. Astruc, R. Y. Chiu, P. T. Nguyen, J. Wang, E. Jue, B. M. Wu, and D. T. Kamei, "Simultaneous concentration and detection of biomarkers on paper," *Lab Chip*, vol. 14, no. 16, pp. 3021–3028, 2014.

[76]   R. C. Wong and H. Y. Tse, *Lateral Flow Immunoassay*. 2009.

[77]   B. Jacono, J. C. Barry, and Q. Corp, "US 9,494,911 B12," *United States Pat.*, 2016.

[78]   K. M. Schilling, A. L. Lepore, J. A. Kurian, and A. W. Martinez, "Fully enclosed microfluidic paper-based analytical devices," *Anal. Chem.*, vol. 84, no. 3, pp. 1579–1585, 2012.

[79]   P. J. Yunker, T. Still, M. a Lohr, and a G. Yodh, "Suppression of the coffee-ring effect by shape-dependent capillary interactions.," *Nature*, vol. 476, no. 7360, pp. 308–311, 2011.

[80]   M. Anyfantakis, Z. Geng, M. Morel, S. Rudiuk, and D. Baigl, "Modulation of the coffee-ring effect in particle/surfactant mixtures: The importance of particle-interface interactions," *Langmuir*, vol. 31, no. 14, pp. 4113–4120, 2015.

[81]   M. Hitzbleck and E. Delamarche, "Reagents in microfluidics: an 'in' and 'out' challenge," *Chem. Soc. Rev.*, vol. 42, no. 21, p. 8494, 2013.